

000 001 002 003 004 005 006 007 008 009 010 011 012 013 014 015 016 017 018 019 020 021 022 023 024 025 026 027 028 029 030 031 032 033 034 035 036 037 038 039 040 041 042 043 044 045 046 047 048 049 050 051 052 053 LORA MEETS SECOND-ORDER OPTIMIZATION: TO- WARDS OPTIMAL LOW-RANK UPDATES

Anonymous authors

Paper under double-blind review

ABSTRACT

Low-rank fine-tuning is widely applied for the effective adaptation of large models. Most existing methods rely on low-rank matrix factorization, whose performance is limited by the condition number of the associated Jacobi operator. Although these methods are computationally efficient, their performance still falls short compared to full fine-tuning. To address this, we propose SoLoRA, which leverages an adaptive metric to find a low-rank approximation of the full fine-tuning gradient. This low-rank approximation can be viewed as an approximation of Hessian, effectively incorporating second-order information to achieve faster convergence and higher optimization efficiency. Furthermore, the low-rank approximation in SoLoRA is computationally simple and easy to implement, achieving a close approximation to the performance of full fine-tuning with almost no additional computational overhead. We conduct fine-tuning experiments on large language models and diffusion models, and the results consistently demonstrate that SoLoRA achieves superior performance advantages over state-of-the-art low-rank fine-tuning methods.

1 INTRODUCTION

Large language models (LLMs) (Liu et al., 2024a; Yang et al., 2024) and vision-language models (Achiam et al., 2023) have demonstrated outstanding performance in various applications, such as chatbot, image generation, and editing. With their strong generalization capabilities and versatility, they have been widely adopted for a range of downstream tasks. To better adapt LLMs to specific downstream tasks, it is often necessary to fine-tune their parameters. However, full fine-tuning is evidently expensive, incurring significant computational and storage costs. To address this, parameter-efficient fine-tuning (PEFT) has emerged to reduce the overhead of fine-tuning.

Low-Rank Adaptation (LoRA) (Hu et al., 2022) is a representative PEFT method. It assumes that weight updates during fine-tuning exhibit a low “intrinsic rank”. By freezing the pretrained weights and introducing two low-rank matrices, $\mathbf{B} \in \mathbb{R}^{m \times r}$ and $\mathbf{A} \in \mathbb{R}^{r \times n}$, for updates, LoRA reduces the number of trainable parameters. Compared to full fine-tuning, the number of trainable parameters in LoRA is $\mathcal{O}((m+n)r)$, where $r \ll \{m, n\}$, significantly lowering the number of trainable parameters, memory consumption, and fine-tuning costs. Owing to these advantages, LoRA and its numerous variants (Hu et al., 2022; Hayou et al., 2024; Zhang and Pilanci, 2024; Wang et al., 2024; Zhao et al., 2024; Zhu et al., 2024; Wang et al., 2025; Mo et al., 2025; Zhang et al., 2025b) have been widely applied in practical applications.

Although LoRA offers significant advantages, most existing fine-tuning algorithms are based on a factorization framework that updates the two low-rank factors separately. Such factorization-based methods are sensitive to the condition number of the low-rank factors, which can result in slow convergence. ScaledGD (Tong et al., 2021; Zhang and Pilanci, 2024) addresses this issue by introducing two preconditioners, effectively eliminating the dependency on the condition number and making its convergence rate condition-number-independent. However, ScaledGD still suffers from parameter redundancy, and its fine-tuning efficiency falls short of matching that of full-parameter fine-tuning.

LoRA-Pro (Wang et al., 2025) demonstrates that applying gradients \mathbf{G}_A and \mathbf{G}_B to the low-rank factors \mathbf{A} and \mathbf{B} is equivalent to performing full fine-tuning on the weight matrix \mathbf{W} with a low-rank gradient $\tilde{\mathbf{G}}$. Building on this insight, LoRA-Pro reduces the discrepancy between $\tilde{\mathbf{G}}$ and the full

054 fine-tuning gradient \mathbf{G} by solving the optimization problem $\min \|\tilde{\mathbf{G}} - \mathbf{G}\|_F^2$, thereby bridging the
 055 performance gap between LoRA and full fine-tuning. LoRA-Pro employs the standard metric inherited
 056 from the Euclidean space of the weight matrices to approximate \mathbf{G} . However, approximation is often
 057 more effective under a weighted metric rather than the standard metric. For example, AdaGrad (Duchi
 058 et al., 2011) and SOAP (Vyas et al., 2025) leverage historical gradient information to adaptively adjust
 059 the step size of each gradient component, effectively utilizing weighted metrics in the Euclidean
 060 space of the weight matrix. K-FAC (Martens and Grosse, 2015; Eschenhagen et al., 2023) uses a
 061 weighted metric based on the Kronecker product to approximate the Hessian, thereby constructing an
 062 efficient preconditioner.

063 Inspired by this, we propose a novel algorithm called **Second-Order Low-Rank Adaption (SoLoRA)**,
 064 which aims to further narrow the performance gap between low-rank fine-tuning and full fine-tuning.
 065 SoLoRA leverages an adaptive metric derived from AdaGrad (Duchi et al., 2011) and SOAP (Vyas
 066 et al., 2025) to identify a low-rank approximation of the full fine-tuning gradient. Notably, this
 067 low-rank approximation can also serve as an approximation of the Hessian, enabling SoLoRA
 068 to effectively incorporate second-order information from the loss function for faster convergence.
 069 Moreover, the optimal low-rank approximation identified by SoLoRA does not directly depend on
 070 the full fine-tuning gradient, making SoLoRA simple and easy to implement. Experiments on GPT-2
 071 and diffusion models demonstrate that SoLoRA, by adopting a weighted metric-based approximation,
 072 outperforms both standard metric-based approximations and existing low-rank fine-tuning methods,
 073 achieving superior performance.

074 2 LOW-RANK FINE-TUNING OF LARGE LANGUAGE MODELS

075 In this section, we revisit existing low-rank fine-tuning methods from a fresh theoretical perspective,
 076 highlighting their gaps compared to full fine-tuning. Based on this analysis, we discuss the limitations
 077 of these low-rank fine-tuning algorithms and elucidate their fundamental distinctions.

078 2.1 RETHINKING LOW-RANK FINE-TUNING: CONNECTIONS AND LIMITATIONS

079 As a representative parameter-efficient fine-tuning method, low-rank fine-tuning works by freezing
 080 the pretrained weights $\mathbf{W}_0 \in \mathbb{R}^{m \times n}$ and assuming that the weight update \mathbf{W} exhibits a low-rank
 081 structure during downstream task adaptation. Consequently, the adaptation process is formulated as a
 082 low-rank constrained optimization problem:

$$083 \min_{\mathbf{W} \in \mathbb{R}^{m \times n}} \mathcal{L}(\mathbf{W}_0 + \mathbf{W}), \quad \text{subject to } \text{rank}(\mathbf{W}) = r,$$

084 where $\mathcal{L}(\cdot)$ denotes the training loss function and $r \ll \min\{m, n\}$. Proximal gradient descent is a
 085 widely adopted method for solving the above low-rank optimization problem by updating the weight
 086 matrix via

$$087 \mathbf{W}_{t+1} = \mathcal{H}_r(\mathbf{W}_t - \alpha_t \nabla_{\mathbf{W}_t} \mathcal{L}(\mathbf{W}_0 + \mathbf{W}_t)),$$

088 where \mathcal{H}_r represents the r -truncated singular value decomposition (SVD) applied to each weight
 089 matrix, α_t is the learning rate of \mathbf{W}_t . This requires performing SVD on every layer at each optimization
 090 step, which has a computational complexity $O(m^3)$, leading to **high-computation cost**.

091 LoRA and its variants (Hu et al., 2022; Wang et al., 2024; Hayou et al., 2024; Liu et al., 2024b; Wang
 092 et al., 2025; Zhang et al., 2025b; Yen et al.; Zhang et al., 2025a) train the network directly via a
 093 low-rank factorization, thereby avoiding the expensive SVD computation at each training step. These
 094 methods aim to solve the following non-convex optimization problem based on the factorization:

$$095 \min_{\mathbf{W} \in \mathbb{R}^{m \times n}} \mathcal{L}(\mathbf{W}_0 + \mathbf{W}), \quad \text{subject to } \mathbf{W} = \mathbf{B}\mathbf{A},$$

096 where $\mathbf{B} \in \mathbb{R}^{m \times r}$, $\mathbf{A} \in \mathbb{R}^{r \times n}$. Here, we define $\mathcal{G}([\mathbf{B}, \mathbf{A}]) = \mathbf{W}$ as a generator that constructs
 097 weight matrices from the low-rank factors. Under this definition, the optimization problem can be
 098 reformulated as:

$$099 \min_{\mathbf{B} \in \mathbb{R}^{m \times r}, \mathbf{A} \in \mathbb{R}^{r \times n}} \mathcal{L}(\mathbf{W}_0 + \mathcal{G}([\mathbf{B}, \mathbf{A}])).$$

100 For factorization-based gradient algorithms, the updates can be expressed as follows, leveraging the
 101 chain rule:

$$102 [\mathbf{B}_{t+1}, \mathbf{A}_{t+1}] = [\mathbf{B}_t, \mathbf{A}_t] - \eta_t J_{\mathcal{G}}^*([\mathbf{B}_t, \mathbf{A}_t]) \nabla_{\mathbf{W}_t} \mathcal{L}(\mathbf{W}_0 + \mathcal{G}([\mathbf{B}_t, \mathbf{A}_t])), \quad (1)$$

108 where $J_{\mathcal{G}}^*$ is the adjoint of the Jacobian operator of \mathcal{G} and η_t is the learning rate of \mathbf{B}_t and \mathbf{A}_t . To
 109 further analyze the gap between low-rank fine-tuning and full fine-tuning, we return to the update of
 110 the weight matrix \mathbf{W} . By applying the generator operator \mathcal{G} to both sides of (1), we get
 111

$$112 \quad \mathcal{G}([\mathbf{B}_{t+1}, \mathbf{A}_{t+1}]) = \mathcal{G}\left([\mathbf{B}_t, \mathbf{A}_t] - \eta_t J_{\mathcal{G}}^*([\mathbf{B}_t, \mathbf{A}_t]) \nabla_{\mathbf{W}_t} \mathcal{L}(\mathbf{W}_0 + \mathcal{G}([\mathbf{B}_t, \mathbf{A}_t]))\right).$$

113 To facilitate comparison with the gradient descent algorithm based on the weight matrix \mathbf{W} , we
 114 perform a Taylor expansion around $[\mathbf{B}_t, \mathbf{A}_t]$,
 115

$$116 \quad \mathbf{W}_{t+1} \approx \mathbf{W}_t - \alpha_t J_{\mathcal{G}}([\mathbf{B}_t, \mathbf{A}_t]) J_{\mathcal{G}}^*([\mathbf{B}_t, \mathbf{A}_t]) \nabla_{\mathbf{W}_t} \mathcal{L}(\mathbf{W}_0 + \mathbf{W}_t), \quad (2)$$

117 where $J_{\mathcal{G}}([\mathbf{B}_t, \mathbf{A}_t])[\cdot, \cdot] : [\mathbb{R}^{m \times r}, \mathbb{R}^{r \times n}] \rightarrow \mathbb{R}^{m \times n}$ is the Jacobian operator. From this update form,
 118 it becomes clear that, compared with full fine-tuning, a key limitation of low-rank fine-tuning lies in
 119 the explicit dependence of the factor gradients on $J_{\mathcal{G}} J_{\mathcal{G}}^*$, whose condition number is determined by
 120 the condition numbers of the low-rank factors \mathbf{B} and \mathbf{A} (Chen et al., 2019; Chi et al., 2019). This
 121 dependency introduces potential instability during training, particularly when fine-tuning complex
 122 neural networks or large language models, which often results in performance degradation (Hayou
 123 et al., 2024; Zhang and Pilanci, 2024).

125 2.2 PRECONDITIONED LOW-RANK ADAPTION FINE-TUNING

126 Under the widely adopted generator form $\mathcal{G}([\mathbf{B}, \mathbf{A}]) = \mathbf{B}\mathbf{A}$, the Jacobian operator $J_{\mathcal{G}}([\mathbf{B}_t, \mathbf{A}_t])[\cdot, \cdot] : \mathbf{P}, \mathbf{Q} \in [\mathbb{R}^{m \times r}, \mathbb{R}^{r \times n}] \rightarrow \mathbb{R}^{m \times n}$ and its adjoint operator $J_{\mathcal{G}}^*([\mathbf{B}_t, \mathbf{A}_t])(\cdot) : \mathbb{R}^{m \times n} \rightarrow [\mathbb{R}^{m \times r}, \mathbb{R}^{r \times n}]$ are
 127 given by
 128

$$J_{\mathcal{G}}([\mathbf{B}_t, \mathbf{A}_t])[\mathbf{P}, \mathbf{Q}] = \mathbf{P}\mathbf{A}_t + \mathbf{B}_t\mathbf{Q},$$

129 for any factor pairs $[\mathbf{P}, \mathbf{Q}] \in [\mathbb{R}^{m \times r}, \mathbb{R}^{r \times n}]$, and
 130

$$J_{\mathcal{G}}^*([\mathbf{B}_t, \mathbf{A}_t])(\mathbf{C}) = [\mathbf{C}\mathbf{A}_t^\top, \mathbf{B}_t^\top\mathbf{C}],$$

131 for any matrices $\mathbf{C} \in \mathbb{R}^{m \times n}$. For detailed derivations and additional information regarding the
 132 Jacobian, please refer to Appendix D.1. Substituting $J_{\mathcal{G}}$ and $J_{\mathcal{G}}^*$ into (2), we can rewrite (2) as
 133

$$\begin{aligned} 134 \quad \mathbf{W}_{t+1} &\approx \mathbf{W}_t - \alpha_t \mathbf{G}_t \cdot \mathbf{A}_t^\top \mathbf{A}_t - \alpha_t \mathbf{B}_t \mathbf{B}_t^\top \cdot \mathbf{G}_t \\ 135 \quad &\approx (\mathbf{B}_t - \eta_t \mathbf{G}_t \cdot \mathbf{A}_t^\top)(\mathbf{A}_t - \eta_t \mathbf{B}_t^\top \cdot \mathbf{G}_t) \\ 136 \quad &= (\mathbf{B}_t - \eta_t \mathbf{G}_{\mathbf{B}_t})(\mathbf{A}_t - \eta_t \mathbf{G}_{\mathbf{A}_t}), \end{aligned}$$

137 where $\mathbf{G}_t = \nabla_{\mathbf{W}_t} \mathcal{L}(\mathbf{W}_0 + \mathbf{W}_t)$, $\mathbf{G}_{\mathbf{B}_t} = \nabla_{\mathbf{B}_t} \mathcal{L}(\mathbf{W}_0 + \mathbf{W}_t)$ and $\mathbf{G}_{\mathbf{A}_t} = \nabla_{\mathbf{A}_t} \mathcal{L}(\mathbf{W}_0 + \mathbf{W}_t)$ are the
 138 gradient of the loss function \mathcal{L} with respect to \mathbf{W}_t , \mathbf{B}_t and \mathbf{A}_t . This formulation aligns with the
 139 update rule of standard LoRA (Vanilla LoRA) (Hu et al., 2022), in which the factors \mathbf{B} and \mathbf{A} are
 140 updated with the same learning rate. Consequently, the convergence rate of standard LoRA depends
 141 on the condition number of $J_{\mathcal{G}}$.
 142

143 To mitigate this dependence on the condition number of $J_{\mathcal{G}}$, several improvements have been proposed.
 144 LoRA+ (Hayou et al., 2024) enhances feature learning efficiency by scaling the update $\eta_t \mathbf{G}_{\mathbf{B}_t}$ with
 145 a factor of 2^4 when training Roberta (Liu et al., 2019) with LeCun initialization (LeCun et al.,
 146 2002). This adjustment can be regarded as applying a constant preconditioner on $\mathbf{G}_{\mathbf{B}_t}$. However,
 147 LoRA+ does not completely eliminate the dependence on the condition number of $J_{\mathcal{G}}$. Imbalance-
 148 Regularized LoRA (Zhu et al., 2024) further alleviates the impact of $J_{\mathcal{G}}$ by introducing regularization
 149 terms on the low-rank factors \mathbf{B}_t and \mathbf{A}_t , which effectively reduce parameter redundancy. Going
 150 further, Riemannian preconditioned LoRA (Zhang and Pilanci, 2024) applies $r \times r$ preconditioners
 151 $(\mathbf{A}_t \mathbf{A}_t^\top)^{-1}$ and $(\mathbf{B}_t^\top \mathbf{B}_t)^{-1}$ to $\mathbf{G}_{\mathbf{B}_t}$ and $\mathbf{G}_{\mathbf{A}_t}$ respectively, making the update of \mathbf{W}_t equivalent to
 152 projecting the gradient onto the row space of \mathbf{A}_t and the column space of \mathbf{B}_t . Specifically,
 153

$$\begin{aligned} 154 \quad \mathbf{B}_{t+1} \mathbf{A}_{t+1} &= (\mathbf{B}_t - \eta_t \mathbf{G}_{\mathbf{B}_t} \cdot (\mathbf{A}_t \mathbf{A}_t^\top)^{-1})(\mathbf{A}_t - \eta_t (\mathbf{B}_t^\top \mathbf{B}_t)^{-1} \cdot \mathbf{G}_{\mathbf{A}_t}) \\ 155 \quad &\approx \mathbf{W}_t - \alpha_t \mathbf{G}_t \cdot \mathbf{A}_t^\top (\mathbf{A}_t \mathbf{A}_t^\top)^{-1} \mathbf{A}_t - \alpha_t \mathbf{B}_t (\mathbf{B}_t^\top \mathbf{B}_t)^{-1} \mathbf{B}_t^\top \cdot \mathbf{G}_t \\ 156 \quad &= \mathbf{W}_t - \alpha_t \text{Proj}_{\text{row}(\mathbf{A}_t)}(\mathbf{G}_t) - \alpha_t \text{Proj}_{\text{col}(\mathbf{B}_t)}(\mathbf{G}_t). \end{aligned}$$

157 Although Riemannian preconditioned LoRA alleviates the influence of condition number of $J_{\mathcal{G}}$ to
 158 some extent via two preconditioners, it still has an important limitation: it ignores the projection
 159 onto the intersection of the row space of \mathbf{A}_t and the column space of \mathbf{B}_t . Specifically, the term

162 $B_t(B_t^\top B_t)^{-1}B_t^\top \cdot G_t \cdot A_t^\top (A_t A_t^\top)^{-1} A_t$ is omitted, which causes the update direction to deviate
 163 from the steepest descent direction. To compensate for the missing information in this cross subspace,
 164 LoRA-Pro (Wang et al., 2025) proposes solving

$$\min_{\Delta_{B_t}, \Delta_{A_t}} \|G_t - (B_t \Delta_{A_t} + \Delta_{B_t} A_t)\|_F^2,$$

165 to more accurately approximate the full fine-tuning gradient and obtain an equivalent low-rank
 166 gradient for the factors B_t and A_t . Optimizing this objective yields the factor updates
 167

$$\begin{cases} \Delta_{B_t} = [I - B_t(B_t^\top B_t)^{-1}B_t^\top]G_t A_t^\top (A_t A_t^\top)^{-1} - B_t X_t, \\ \Delta_{A_t} = (B_t^\top B_t)^{-1}B_t^\top G_t + X_t A_t, \end{cases}$$

170 for some $X_t \in \mathbb{R}^{r \times r}$. The corresponding update of the weight matrix is
 171

$$\begin{aligned} & B_t \Delta_{A_t} + \Delta_{B_t} A_t \\ &= B_t(B_t^\top B_t)^{-1}B_t^\top G_t + B_t X_t A_t + [I - B_t(B_t^\top B_t)^{-1}B_t^\top]G_t A_t^\top (A_t A_t^\top)^{-1} A_t - B_t X_t A_t \\ &= (B_t(B_t^\top B_t)^{-1}B_t^\top)G_t + G_t(A_t^\top (A_t A_t^\top)^{-1} A_t) - (B_t(B_t^\top B_t)^{-1}B_t^\top)G_t(A_t^\top (A_t A_t^\top)^{-1} A_t) \\ &= \text{Proj}_{\text{col}(B_t)}(G_t) + \text{Proj}_{\text{row}(A_t)}(G_t) - \text{Proj}_{\text{col}(B_t) \cap \text{row}(A_t)}(G_t) = \mathcal{P}_{\mathbb{T}_t}(G_t). \end{aligned} \tag{3}$$

173 where \mathcal{M}_r is the Riemannian manifold of all rank r matrices, and \mathbb{T}_t denotes the tangent space of
 174 \mathcal{M}_r at the point W_t . By Proposition D.2, $\mathcal{P}_{\mathbb{T}_t}(G_t)$ is the orthogonal projection of G_t onto \mathbb{T}_t .
 175

176 Although LoRA-Pro is capable of finding a low-rank approximation of the full fine-tuning gradient
 177 under a standard metric, it incurs higher computational overhead due to solving a Sylvester equation
 178 at each step. (Lu, 1971; Dmytryshyn et al., 2025). In comparison, gradient approximations based
 179 on weighted metrics are often more effective, as they better utilize the second-order information of
 180 the loss function. For instance, classical methods such as the Broyden–Fletcher–Goldfarb–Shanno
 181 (BFGS) algorithm (Fletcher, 2000) and the Gauss–Newton method (Nocedal and Wright, 2006)
 182 both benefit from weighted metrics. Previous research has demonstrated that weighted metrics can
 183 significantly enhance algorithmic efficiency across a variety of problems (Duchi et al., 2011; Bian
 184 et al., 2024). Motivated by this, we propose designing a novel weighted metric to further improve
 185 the approximation of full fine-tuning gradients and to fully exploit the second-order information
 186 embedded in the loss function, enabling a more effective low-rank approximation.
 187

3 THE PROPOSED ALGORITHMS

188 Empirical evidence suggests that the weighted metric are often more effective than the standard
 189 metric in deep learning. For instance, AdaGrad (Duchi et al., 2011; Shazeer and Stern, 2018) and
 190 SOAP (Gupta et al., 2018; Morwani et al., 2024; Vyas et al., 2025) adaptively adjust the step size
 191 of each gradient component based on historical gradient information, which is equivalent to using a
 192 weighted metric for the weight matrix. Similarly, K-FAC (Martens and Grosse, 2015; Eschenhagen
 193 et al., 2023) employs a Kronecker product-based weighted metric to approximate the Hessian, thereby
 194 constructing an efficient preconditioner. In this section, we introduce a novel weighted metric and
 195 derive a low-rank approximation of the full fine-tuning gradient G based on this metric. This low-
 196 rank approximation can be viewed as an approximation of the Hessian, allowing our algorithm to
 197 effectively exploit the second-order information of the loss function, thereby narrowing the gap
 198 between the performance of low-rank fine-tuning and full fine-tuning.
 199

3.1 CONSTRUCTION OF THE ADAPTIVE METRIC

200 The core idea of AdaGrad (Duchi et al., 2011) and Adam (Kingma and Ba, 2014) is to construct a
 201 weighted operator h_t through the outer product of gradients, followed by a diagonalization operation.
 202 Specifically, by vectorizing the gradient matrix $G_t \in \mathbb{R}^{m \times n}$ into $g_t \in \mathbb{R}^{mn \times 1}$, the linearized
 203 weighted operator h_t is denoted as $h_t = (h_{t-1}^2 + \text{diag}(g_t g_t^\top))^{\frac{1}{2}}$, where $\text{diag}(\cdot)$ extracts the diagonal
 204 elements of the matrix. This operator h_t is then used to define a new weighted inner product, under
 205 which the gradient descent update to linearized weight w_t is derived $w_{t+1} = w_t - g_t/h_t$. AdaGrad
 206 employs the elements of h_t to rescale the gradient element-wise. However, when applied to gradient
 207

updates in matrix form, this element-wise rescaling approach ignores the structural information of the matrix, i.e., the relationships between rows and columns. To better utilize matrix structures, Shampoo (Gupta et al., 2018) adopts the Kronecker product to approximate the construction of the weighted matrix. Specifically, Shampoo constructs two matrices, $\mathbf{L}_t = \mathbf{L}_{t-1} + \mathbf{G}_t \mathbf{G}_t^\top$ and $\mathbf{R}_t = \mathbf{R}_{t-1} + \mathbf{G}_t^\top \mathbf{G}_t$, and defines a weighted inner product based on these matrices. Under this inner product, the matrix update is performed by $\mathbf{W}_{t+1} = \mathbf{W}_t - \mathbf{L}_t^{-\frac{1}{4}} \mathbf{G}_t \mathbf{R}_t^{-\frac{1}{4}}$. SOAP (Morwani et al., 2024; Vyas et al., 2025) further improves upon Shampoo by noting that the square root operation in Shampoo is equivalent to running Adafactor (Shazeer and Stern, 2018) in the eigenbasis of the Shampoo preconditioner. To enhance the computational efficiency of Shampoo, SOAP runs Adam in the eigenbasis of the Shampoo preconditioner. However, frequent eigen-decomposition computations result in high computational costs. To balance leveraging matrix structural information and maintaining computational efficiency, we propose a hybrid weighted inner product that is easier to implement, better aligns with matrix structures, and fully utilizes the relationships between matrix rows and columns.

Specifically, we define the weighted factors \mathbf{L}_t and \mathbf{R}_t as follows:

$$\begin{aligned} \mathbf{L}_t &= \text{diag}(\mathbf{l}_t / \sqrt{\|\mathbf{l}_t\|_1}) \text{ with } \mathbf{l}_t = \beta_1 \mathbf{l}_{t-1} + (1 - \beta_1) \sum_{j=1}^n (\mathbf{G}_t \odot \mathbf{G}_t)_{i,j}, \\ \mathbf{R}_t &= \text{diag}(\mathbf{r}_t / \sqrt{\|\mathbf{r}_t\|_1}) \text{ with } \mathbf{r}_t = \beta_2 \mathbf{r}_{t-1} + (1 - \beta_2) \sum_{i=1}^m (\mathbf{G}_t \odot \mathbf{G}_t)_{i,j}, \end{aligned} \quad (4)$$

where \odot denotes the Hadamard (element-wise) product, $\|\cdot\|_1$ denotes the l_1 -norm, β_1, β_2 are decay factors in the range $[0, 1]$. The term $\sum_{j=1}^n (\mathbf{G}_t \odot \mathbf{G}_t)_{i,j}$ forms a vector of the diagonal elements of the matrix $\mathbf{G}_t \mathbf{G}_t^\top$, and similarly, $\sum_{i=1}^m (\mathbf{G}_t \odot \mathbf{G}_t)_{i,j}$ forms a vector of the diagonal elements of the matrix $\mathbf{G}_t^\top \mathbf{G}_t$. As stated in (Shazeer and Stern, 2018), $\mathbf{l}_t \mathbf{r}_t^\top$ is a rank-1 approximation of $\mathbf{G} \odot \mathbf{G}$, which is optimal with respect to the generalized Kullback-Leibler divergence. In this way, the memory requirement is reduced from $\mathcal{O}(mn)$ to $\mathcal{O}(m + n)$. At the same time, compared to Shampoo, the computational complexity of \mathbf{L}_t and \mathbf{R}_t is reduced to $\mathcal{O}(mn)$.

Based on \mathbf{L}_t and \mathbf{R}_t , we define an adaptive weighted inner product in $\mathbb{R}^{m \times n}$. For any $\mathbf{Y}, \mathbf{Z} \in \mathbb{R}^{m \times n}$, the adaptive weighted inner product is given by:

$$\langle \mathbf{Y}, \mathbf{Z} \rangle_{\mathbf{H}_t} = \langle \mathbf{H}_t \mathbf{Y}, \mathbf{Z} \rangle = \langle \mathbf{L}_t^{\frac{1}{2}} \mathbf{Y} \mathbf{R}_t^{\frac{1}{2}}, \mathbf{Z} \rangle. \quad (5)$$

For any matrix $\mathbf{K} \in \mathbb{R}^{m \times n}$, the inverse operation of the operator \mathbf{H}_t is defined as

$$\mathbf{H}_t^{-1} \mathbf{K} = \mathbf{L}_t^{-\frac{1}{2}} \mathbf{K} \mathbf{R}_t^{-\frac{1}{2}}.$$

3.2 SECOND-ORDER LOW-RANK ADAPTION FOR FINE-TUNING

Based on the adaptive weighted inner product, we aim to incorporate second-order information into the update of the weight matrix \mathbf{W} . To achieve this, we consider the update of the weight matrix \mathbf{W} in step t . Let the update to \mathbf{W} at step t be denoted as Δ_t . In this step, we solve the problem:

$$\min_{\Delta_t} \mathcal{L}((\mathbf{W}_0 + \mathbf{W}_t) - \Delta_t).$$

We then expand the loss function $\mathcal{L}(\mathbf{W})$ around the point $\mathbf{W}_0 + \mathbf{W}_t$ using its second-order Taylor expansion. By utilizing the weighted inner product as an approximation of Hessian, the optimization problem can be formulated as:

$$\begin{aligned} &\arg \min_{\Delta_t} \mathcal{L}((\mathbf{W}_0 + \mathbf{W}_t) - \Delta_t) \\ &\approx \arg \min_{\Delta_t} \mathcal{L}(\mathbf{W}_0 + \mathbf{W}_t) - \langle \Delta_t, \mathbf{G}_t \rangle + \frac{1}{2} \langle \mathbf{H}_t \Delta_t, \Delta_t \rangle, \\ &= \arg \min_{\Delta_t} \mathcal{L}(\mathbf{W}_0 + \mathbf{W}_t) - \langle \Delta_t, \mathbf{H}_t^{-1} \mathbf{G}_t \rangle_{\mathbf{H}_t} + \frac{1}{2} \langle \Delta_t, \Delta_t \rangle_{\mathbf{H}_t} + \frac{1}{2} \langle \mathbf{H}_t^{-1} \mathbf{G}_t, \mathbf{H}_t^{-1} \mathbf{G}_t \rangle_{\mathbf{H}_t} \\ &= \arg \min_{\Delta_t} \mathcal{L}(\mathbf{W}_0 + \mathbf{W}_t) + \frac{1}{2} \|\Delta_t - \mathbf{H}_t^{-1} \mathbf{G}_t\|_{\mathbf{H}_t}^2. \end{aligned}$$

From this expression, it is evident that the optimization problem is equivalent to finding the optimal Δ_t for the following objective:

$$\min_{\Delta_t} \|\Delta_t - \mathbf{H}_t^{-1} \mathbf{G}_t\|_{\mathbf{H}_t}^2. \quad (6)$$

Let the optimal update be denoted as Δ_t^{opt} . From the form of (6), it becomes clear that Δ_t^{opt} serves as an approximation of the Newton direction

$$-\Delta_t^{\text{opt}} \approx -\nabla^2 \mathcal{L}(\mathbf{W}_0 + \mathbf{W}_t) \cdot \nabla \mathcal{L}(\mathbf{W}_0 + \mathbf{W}_t).$$

Thus, the weight matrix is updated as $\mathbf{W}_{t+1} = \mathbf{W}_t - \Delta_t^{\text{opt}}$. The advantages of this update are evident:

- It completely eliminates the adverse effects of the condition number of the Jacobian operator $J_{\mathcal{G}}$, thereby improving the stability of the algorithm.
- It effectively incorporates the second-order information of the loss function, enhancing optimization efficiency.

To further reduce memory consumption, we adopt the low-rank factorization strategy of LoRA, representing the update Δ_t in terms of updates to the low-rank factors \mathbf{A}_t and \mathbf{B}_t , denoted as $\Delta_{\mathbf{A}_t}$ and $\Delta_{\mathbf{B}_t}$, respectively. As noted in (Wang et al., 2025), the changes in the factors \mathbf{A}_t and \mathbf{B}_t are intrinsically related to the updates in the weight matrix \mathbf{W}_t , which can be expressed as

$$\Delta_t = \Delta_{\mathbf{B}_t} \mathbf{A}_t + \mathbf{B}_t \Delta_{\mathbf{A}_t}.$$

Therefore, the minimization problem (6) can be equivalently transformed into:

$$\min_{\Delta_{\mathbf{B}_t}, \Delta_{\mathbf{A}_t}} \|\Delta_{\mathbf{B}_t} \mathbf{A}_t + \mathbf{B}_t \Delta_{\mathbf{A}_t} - \mathbf{H}_t^{-1} \mathbf{G}_t\|_{\mathbf{H}_t}^2. \quad (7)$$

To make the optimization process more explicit, we first rewrite (7) as:

$$\begin{aligned} & \arg \min_{\Delta_{\mathbf{B}_t}, \Delta_{\mathbf{A}_t}} \|\tilde{\mathcal{P}}_{\mathbb{T}_t}(\Delta_{\mathbf{B}_t} \mathbf{A}_t + \mathbf{B}_t \Delta_{\mathbf{A}_t} - \mathbf{H}_t^{-1} \mathbf{G}_t) + \tilde{\mathcal{P}}_{\mathbb{T}_t}^\perp(\Delta_{\mathbf{B}_t} \mathbf{A}_t + \mathbf{B}_t \Delta_{\mathbf{A}_t} - \mathbf{H}_t^{-1} \mathbf{G}_t)\|_{\mathbf{H}_t}^2 \\ &= \arg \min_{\Delta_{\mathbf{B}_t}, \Delta_{\mathbf{A}_t}} \|\Delta_{\mathbf{B}_t} \mathbf{A}_t + \mathbf{B}_t \Delta_{\mathbf{A}_t} - \tilde{\mathcal{P}}_{\mathbb{T}_t}(\mathbf{H}_t^{-1} \mathbf{G}_t)\|_{\mathbf{H}_t}^2 + \|\tilde{\mathcal{P}}_{\mathbb{T}_t}^\perp(\mathbf{H}_t^{-1} \mathbf{G}_t)\|_{\mathbf{H}_t}^2, \end{aligned} \quad (8)$$

where $\tilde{\mathcal{P}}_{\mathbb{T}_t}^\perp(\cdot)$ denotes the projection onto the space orthogonal to the tangent space. This equivalence holds because $\Delta_{\mathbf{B}_t} \mathbf{A}_t + \mathbf{B}_t \Delta_{\mathbf{A}_t}$ lies in the tangent space \mathbb{T}_t (see Proposition D.4). This implies that, to find the optimal $\Delta_{\mathbf{B}_t}$ and $\Delta_{\mathbf{A}_t}$, we ultimately need to solve the following equivalent problem:

$$\min_{\Delta_{\mathbf{B}_t}, \Delta_{\mathbf{A}_t}} \|\Delta_{\mathbf{B}_t} \mathbf{A}_t + \mathbf{B}_t \Delta_{\mathbf{A}_t} - \tilde{\mathcal{P}}_{\mathbb{T}_t}(\mathbf{H}_t^{-1} \mathbf{G}_t)\|_{\mathbf{H}_t}^2. \quad (9)$$

Here, $\tilde{\mathcal{P}}_{\mathbb{T}_t}(\mathbf{H}_t^{-1} \mathbf{G}_t)$ represents the projection of $\mathbf{H}_t^{-1} \mathbf{G}_t$ onto \mathbb{T}_t , with its explicit form given as

$$\tilde{\mathcal{P}}_{\mathbb{T}_t}(\mathbf{L}_t^{-\frac{1}{2}} \mathbf{G}_t \mathbf{R}_t^{-\frac{1}{2}}) = \tilde{\mathcal{P}}_{\mathbf{B}_t} \mathbf{L}_t^{-\frac{1}{2}} \mathbf{G}_t \mathbf{R}_t^{-\frac{1}{2}} + \mathbf{L}_t^{-\frac{1}{2}} \mathbf{G}_t \mathbf{R}_t^{-\frac{1}{2}} \tilde{\mathbf{Q}}_{\mathbf{A}_t} - \tilde{\mathcal{P}}_{\mathbf{B}_t} \mathbf{L}_t^{-\frac{1}{2}} \mathbf{G}_t \mathbf{R}_t^{-\frac{1}{2}} \tilde{\mathbf{Q}}_{\mathbf{A}_t}, \quad (10)$$

where $\tilde{\mathcal{P}}_{\mathbf{B}_t} = \mathbf{B}_t (\mathbf{B}_t^\top \mathbf{L}_t^{\frac{1}{2}} \mathbf{B}_t)^{-1} \mathbf{B}_t^\top \mathbf{L}_t^{\frac{1}{2}}$ and $\tilde{\mathbf{Q}}_{\mathbf{A}_t} = \mathbf{R}_t^{\frac{1}{2}} \mathbf{A}_t^\top (\mathbf{A}_t \mathbf{R}_t^{\frac{1}{2}} \mathbf{A}_t^\top)^{-1} \mathbf{A}_t$. The detailed derivation is provided in Appendix D.3.

For problem (9), we provide its explicit solution in the following Theorem 3.1. For the proof of Theorem 3.1, please refer to Appendix D.3.

Theorem 3.1 (Optimal updates for low-rank factors). *Let $\mathbf{W}_t = \mathbf{B}_t \mathbf{A}_t$ be a rank- r factorization at t -th step, and let $\tilde{\mathcal{P}}_{\mathbb{T}_t}(\mathbf{L}_t^{-\frac{1}{2}} \mathbf{G}_t \mathbf{R}_t^{-\frac{1}{2}})$ denote the projection of the preconditioned gradient $\mathbf{L}_t^{-\frac{1}{2}} \mathbf{G}_t \mathbf{R}_t^{-\frac{1}{2}}$ onto the tangent space \mathbb{T}_t at \mathbf{W}_t . Consider the following optimization problem:*

$$\min_{\Delta_{\mathbf{B}_t}, \Delta_{\mathbf{A}_t}} \frac{1}{2} \|\Delta_{\mathbf{B}_t} \mathbf{A}_t + \mathbf{B}_t \Delta_{\mathbf{A}_t} - \tilde{\mathcal{P}}_{\mathbb{T}_t}(\mathbf{L}_t^{-\frac{1}{2}} \mathbf{G}_t \mathbf{R}_t^{-\frac{1}{2}})\|_{\mathbf{H}_t}^2, \quad (11)$$

where $\|\cdot\|_{\mathbf{H}_t}$ is the norm induced by the operator \mathbf{H}_t . Then the optimal solutions for $\Delta_{\mathbf{B}_t}$ and $\Delta_{\mathbf{A}_t}$ are given by

$$\Delta_{\mathbf{B}_t}^{\text{opt}} = [\mathbf{I} - \mathbf{B}_t (\mathbf{B}_t^\top \mathbf{L}_t^{\frac{1}{2}} \mathbf{B}_t)^{-1} \mathbf{B}_t^\top \mathbf{L}_t^{\frac{1}{2}}] \mathbf{L}_t^{-\frac{1}{2}} \mathbf{G}_{\mathbf{B}_t} (\mathbf{A}_t \mathbf{R}_t^{\frac{1}{2}} \mathbf{A}_t^\top)^{-1} - \mathbf{B}_t \mathbf{X}_t,$$

$$\Delta_{\mathbf{A}_t}^{\text{opt}} = (\mathbf{B}_t^\top \mathbf{L}_t^{\frac{1}{2}} \mathbf{B}_t)^{-1} \mathbf{G}_{\mathbf{A}_t} \mathbf{R}_t^{-\frac{1}{2}} + \mathbf{X}_t \mathbf{A}_t,$$

where $\mathbf{X}_t \in \mathbb{R}^{r \times r}$ is an arbitrary matrix.

From Theorem 3.1, we observe that although G_t appears in the solution, it does not directly appear in the closed-form expression. Instead, the solution depends on the low-rank gradients G_{A_t} and G_{B_t} , ensuring low memory overhead. This efficient representation allows for straightforward gradient updates: first, compute the gradients using standard backpropagation, and then adjust Δ_{B_t} and Δ_{A_t} according to the closed-form solution. While Δ_{B_t} and Δ_{A_t} depend on X_t , the choice of X_t is critical for balancing the updates. Next, we minimize the weighted norm of the difference between the two update components, $\Delta_{B_t} A_t$ and $B_t \Delta_{A_t}$. This yields the optimal X_t in Theorem 3.2 (proof provided in Appendix D.3).

Once the matrix X_t is computed, Δ_{B_t} and Δ_{A_t} can be derived. Using the updates Δ_{B_t} and Δ_{A_t} , we propose **Second-order Low-Rank Adaption (SoLoRA)**, summarized in Algorithm 1. The computational complexity is analyzed in Appendix C.

Theorem 3.2 (Optimal Solution for Balancing Matrix X_t). *Let $X_t \in \mathbb{R}^{r \times r}$. Consider the following optimization problem with respect to X_t ,*

$$\min_{X_t \in \mathbb{R}^{r \times r}} \frac{1}{2} \|\Delta_{B_t} A_t - B_t \Delta_{A_t}\|_{H_t}^2, \quad (12)$$

where Δ_{B_t} and Δ_{A_t} are functions of X_t given in Theorem 3.1. Then the optimal solution for X_t is given by

$$X_t^{opt} = -\frac{1}{2} (B_t^\top L_t^{\frac{1}{2}} B_t)^{-1} B_t^\top G_t A_t^\top (A_t R_t^{\frac{1}{2}} A_t^\top)^{-1}.$$

Algorithm 1 Second-order Low-Rank Adaption (SoLoRA) with SGD for Fine-tuning.

```

1: Initialize  $B_1 = \mathbf{0}_{m \times r}$ ,  $A_1 = \text{Kaiming uniform}_{r \times n}$ ,  $l_0 = \mathbf{0}_m$ ,  $r_0 = \mathbf{0}_n$ ,  $\epsilon = 1e-6$ .
2: for  $t = 1, \dots, T$  do
3:    $l_t = \beta_1 l_{t-1} + (1 - \beta_1) \sum_{j=1}^n (G_t \odot G_t)_{i,j}$ ,  $L_t = \text{diag}(l_t / \sqrt{\|l_t\|_1})$ .
4:    $r_t = \beta_2 r_{t-1} + (1 - \beta_2) \sum_{i=1}^m (G_t \odot G_t)_{i,j}$ ,  $R_t = \text{diag}(r_t / \sqrt{\|r_t\|_1})$ .
5:    $\Delta_{B_t} = \left[ I - \frac{1}{2} B_t (B_t^\top L_t^{\frac{1}{2}} B_t)^{-1} B_t^\top L_t^{\frac{1}{2}} \right] L_t^{-\frac{1}{2}} G_{B_t} (A_t R_t^{\frac{1}{2}} A_t^\top)^{-1}$ .
6:    $\Delta_{A_t} = (B_t^\top L_t^{\frac{1}{2}} B_t)^{-1} G_{A_t} R_t^{-\frac{1}{2}} \left[ I - \frac{1}{2} R_t^{\frac{1}{2}} A_t^\top (A_t R_t^{\frac{1}{2}} A_t^\top)^{-1} A_t \right]$ .
7:    $B_{t+1} = B_t - \eta_t \Delta_{B_t}$ ,  $A_{t+1} = A_t - \eta_t \Delta_{A_t}$ .
8: end for
9: Note: Add  $\epsilon I$  to matrix  $B_t^\top L_t^{\frac{1}{2}} B_t$  if it is not invertible.

```

3.3 SECOND-ORDER LOW-RANK ADAPTION WITH MOMENTUM FOR FINE-TUNING.

First-order momentum methods, such as Adam and AdamW (Kingma and Ba, 2014; Loshchilov and Hutter, 2017), have been shown to be highly effective in stochastic optimization. By maintaining an exponential moving average of both the per-coordinate gradient statistics and the raw gradients, Adam stabilizes updates, reduces gradient variance, and minimizes sensitivity to manual learning rate tuning. To incorporate these advantages into our second-order low-rank adaptation framework, we integrate the exponential moving average of the gradients into SoLoRA. The enhanced method preserves the curvature-aware geometric properties of SoLoRA while inheriting the stability and adaptivity of Adam, resulting in more reliable and efficient fine-tuning. The pseudocode is present in Algorithm 2.

4 EXPERIMENTAL RESULTS

To evaluate the performance of our SoLoRA algorithm, we apply it to fine-tuning tasks for the large language model GPT-2 (see Section 4.1 and Appendix A) and diffusion models (see Appendix B). In the experiments, we compare two kinds of optimization algorithms: SGD-based algorithms and AdamW-based algorithms. The SGD-based algorithms include: LoRA with SGD optimizer (referred to as SGD) (Hu et al., 2022), Scaled GD (Zhang and Pilanci, 2024; Tong et al., 2021), LoRA-Pro with SGD optimizer (Wang et al., 2025), and our SoLoRA with SGD optimizer (Algorithm 1). The AdamW-based algorithms include: LoRA with AdamW optimizer (referred to as AdamW) (Hu et al.,

378 **Algorithm 2** Second-order Low-Rank Adaption (SoLoRA) with Momentum for Fine-tuning.

379

380 1: Initialize moment $M_0 = \mathbf{0}_{m \times n}$, $B_1 = \mathbf{0}_{m \times r}$, $A_1 = \text{Kaiming uniform}_{r \times n}$; $l_0 = \mathbf{0}_m$, $r_0 = \mathbf{0}_n$,

381 weight decay λ , coefficients $\beta_1 = \beta_2$, and β_3 , $\epsilon = 1e - 6$.

382 2: **for** $t = 1, \dots, T$ **do**

383 3: $l_t = \beta_1 l_{t-1} + (1 - \beta_1) \sum_{j=1}^n (G_t \odot G_t)_{i,j}$, $L_t = \text{diag}(l_t / \sqrt{\|l_t\|_1})$.

384 4: $r_t = \beta_2 r_{t-1} + (1 - \beta_2) \sum_{i=1}^m (G_t \odot G_t)_{i,j}$, $R_t = \text{diag}(r_t / \sqrt{\|r_t\|_1})$.

385 5: $M_t = \beta_3 M_{t-1} + (1 - \beta_3) G_t$.

386 6: $\Delta_{B_t} = \left[I - \frac{1}{2} B_t \left(B_t^\top L_t^{\frac{1}{2}} B_t \right)^{-1} B_t^\top L_t^{\frac{1}{2}} \right] L_t^{-\frac{1}{2}} M_t A_t^\top \left(A_t R_t^{\frac{1}{2}} A_t^\top \right)^{-1}$.

387 7: $\Delta_{A_t} = \left(B_t^\top L_t^{\frac{1}{2}} B_t \right)^{-1} B_t^\top M_t R_t^{-\frac{1}{2}} \left[I - \frac{1}{2} R_t^{\frac{1}{2}} A_t^\top \left(A_t R_t^{\frac{1}{2}} A_t^\top \right)^{-1} A_t \right]$.

388 8: $B_{t+1} = (1 - \lambda \eta_t) B_t - \eta_t \frac{\sqrt{1 - \beta_1^t}}{1 - \beta_3^t} \Delta_{B_t}$, $A_{t+1} = (1 - \lambda \eta_t) A_t - \eta_t \frac{\sqrt{1 - \beta_1^t}}{1 - \beta_3^t} \Delta_{A_t}$.

389 9: **end for**

390 10: **Note:** Add ϵI to matrix $B_t^\top L_t^{\frac{1}{2}} B_t$ if it is not invertible.

394

395 2022), Scaled AdamW (Zhang and Pilanci, 2024), LoRA-Pro with AdamW optimizer (Wang et al.,

396 2025), and our SoLoRA with AdamW optimizer (Algorithm 2). All experiments are implemented

397 using PyTorch (Paszke et al., 2019) and conducted on NVIDIA GeForce RTX 4090 or 3090 GPUs.

398

399 4.1 GPT-2 FINE-TUNING

400

401 In this section, we conduct fine-tuning experiments on the GPT-2 model (Radford et al., 2019) using

402 SoLoRA. First, we perform fine-tuning on the GPT-2 small model with ranks 16 and 64, evaluated

403 on the E2E natural language generation challenge (Novikova et al., 2017). The results are shown

404 in Table 1. The experimental setup follows (Zhang and Pilanci, 2024), but we independently tune

405 the learning rate for each optimizer using grid search. As shown in Table 1, the model trained with

406 SoLoRA outperforms all other methods across all evaluation metrics, regardless of whether the SGD

407 or AdamW optimizer is used. To further validate the efficiency of SoLoRA, we compare the loss

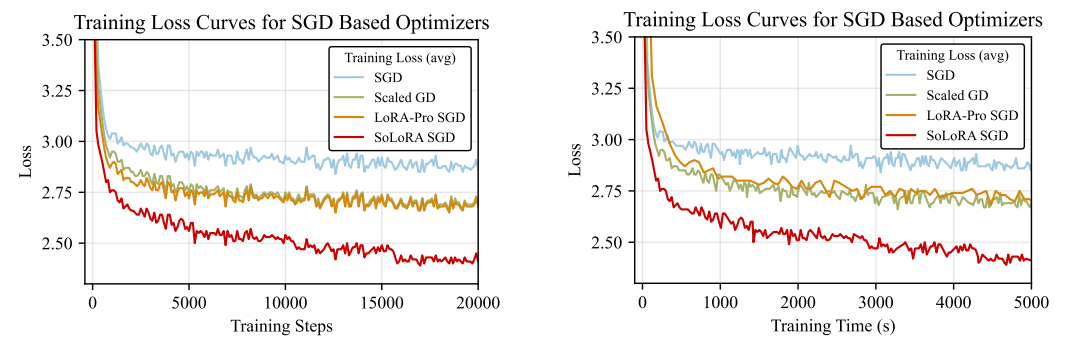
408 reduction trends when employing different optimizers under the same runtime and the same number

409 of iterations. These results are illustrated in Figures 1 and 2. The findings demonstrate that SoLoRA

410 achieves significantly faster loss reduction than other algorithms within the same runtime, thanks to

411 its effective utilization of second-order information of the loss function.

412



423 (a) Training loss curve over training step when fine-
424 tuning using SGD-based methods.

425 (b) Training loss curve over training time when fine-
426 tuning using SGD-based methods.

427 Figure 1: Training loss GPT-2 small model ($r = 64$) fine-tuned using different SGD-based optimizers.
428 Evaluation is conducted on E2E Natural Language Generation Challenge.

429 Optimizing low-rank factorization matrices presents inherent challenges, particularly when the weight

430 matrix contains small singular values — a scenario that often arises with larger ranks, such as ranks

431 16 and 64 in this experiment. Under these conditions, the curvature of Hessian becomes very large,

432 resulting in a high condition number and making the optimization problem ill-conditioned. Despite

these challenges, SoLoRA demonstrates superior performance in both computational efficiency and final evaluation metrics. This highlights the ability of SoLoRA to effectively mitigate the impact of J_g 's condition number while leveraging the second-order information from the loss function. To further evaluate SoLoRA, we conducted additional experiments on GPT-2 models of varying sizes with rank 4. The results are presented in Table 2 (see Appendix A), reaffirm the advantages of SoLoRA. Finally, we test the stability of SoLoRA under different learning rates, with the results shown in Figure 3 (see Appendix A). The experiments reveal that, compared to other algorithms, SoLoRA exhibits greater stability across varying ranks and learning rates.

Table 1: Scores of GPT-2 small model fine-tuned using different optimizers. Evaluation is conducted on E2E Natural Language Generation challenge.

rank	Method	E2E				
		BLEU	NIST	MET	ROUGE-L	CIDEr
16	SGD	65.4	8.07	40.7	67.0	2.07
	Scaled GD	68.8	8.75	45.0	69.2	2.39
	LoRA-Pro SGD	68.3	8.67	45.1	69.3	2.37
	SoLoRA SGD (ours)	70.0	8.82	46.6	71.6	2.53
	AdamW	69.5	8.77	46.4	71.2	2.48
64	Scaled AdamW	69.8	8.79	46.5	71.7	2.51
	LoRA-Pro AdamW	69.7	8.73	46.8	71.7	2.51
	SoLoRA AdamW (ours)	70.2	8.85	46.6	71.9	2.52
	SGD	64.7	8.08	40.8	66.7	2.04
	Scaled GD	68.5	8.68	45.0	69.4	2.38
256	LoRA-Pro SGD	68.6	8.71	45.4	69.7	2.38
	SoLoRA SGD (ours)	70.1	8.85	46.7	71.8	2.53
	AdamW	69.6	8.76	46.7	71.5	2.50
	Scaled AdamW	70.0	8.83	46.4	71.5	2.50
	LoRA-Pro AdamW	70.0	8.82	46.6	71.5	2.51
512	SoLoRA AdamW (ours)	70.2	8.84	46.8	72.1	2.52

5 CONCLUSION

This paper addresses the performance limitations of low-rank fine-tuning in efficiently adapting large models by proposing the second-order low-rank adaptation algorithm, **SoLoRA**. SoLoRA leverages an adaptive metric inspired by AdaGrad (Duchi et al., 2011) and SOAP (Vyas et al., 2025) to efficiently compute a low-rank approximation of the full fine-tuning gradient. This approximation, which can be viewed as an approximation of Hessian, effectively incorporates second-order information, accelerating convergence and improving optimization efficiency. Compared to existing low-rank fine-tuning methods, SoLoRA not only exploits second-order information but also completely eliminates the impact of the condition number of Jacobian operator. Moreover, as its low-rank approximation does not directly depend on the full gradient, SoLoRA is simpler and more efficient to implement. Experiments on GPT-2 and diffusion models consistently demonstrate that SoLoRA outperforms state-of-the-art low-rank fine-tuning methods. It achieves performance close to full fine-tuning while incurring almost no additional computational cost. This strongly demonstrates that second-order low-rank approximations based on our adaptive weighted metric provide a practical path to bridging the gap between parameter efficiency and optimal performance, paving the way for efficient and robust task transfer and personalized customization in large models.

Ethics statement This paper conforms with the ICLR Code of Ethics.

Reproducibility statement We are committed to the reproducibility of our research. To this end, we have made all source code, environmental configurations, and data access instructions available in the supplementary material. Furthermore, the key parameters for our experiments are provided in Table 3, Table 4, and Table 6 to facilitate the replication of our findings.

486 REFERENCES
487

488 P-A Absil, Robert Mahony, and Rodolphe Sepulchre. Optimization algorithms on matrix manifolds. In
489 *Optimization Algorithms on Matrix Manifolds*. Princeton University Press, 2009.

490 Josh Achiam, Steven Adler, Sandhini Agarwal, Lama Ahmad, Ilge Akkaya, Florencia Leoni Aleman, Diogo
491 Almeida, Janko Altenschmidt, Sam Altman, Shyamal Anadkat, et al. Gpt-4 technical report. *arXiv preprint*
492 *arXiv:2303.08774*, 2023.

493 Fengmiao Bian, Jian-Feng Cai, and Rui Zhang. A preconditioned riemannian gradient descent algorithm for
494 low-rank matrix recovery. *SIAM Journal on Matrix Analysis and Applications*, 45(4):2075–2103, 2024.

495 Yuxin Chen, Yuejie Chi, Jianqing Fan, and Cong Ma. Gradient descent with random initialization: Fast global
496 convergence for nonconvex phase retrieval. *Mathematical Programming*, 176(1):5–37, 2019.

497 Yuejie Chi, Yue M Lu, and Yuxin Chen. Nonconvex optimization meets low-rank matrix factorization: An
498 overview. *IEEE Transactions on Signal Processing*, 67(20):5239–5269, 2019.

499 Andrii Dmytryshyn, Massimiliano Fasi, Nicholas J Higham, and Xiaobo Liu. Mixed-precision algorithms for
500 solving the sylvester matrix equation. *arXiv preprint arXiv:2503.03456*, 2025.

501 John Duchi, Elad Hazan, and Yoram Singer. Adaptive subgradient methods for online learning and stochastic
502 optimization. *Journal of Machine Learning Research*, 12(7), 2011.

503 Runa Eschenhagen, Alexander Immer, Richard Turner, Frank Schneider, and Philipp Hennig. Kronecker-
504 factored approximate curvature for modern neural network architectures. In *Advances in Neural Information
505 Processing Systems (NIPS)*, volume 36, pages 33624–33655, 2023.

506 Roger Fletcher. *Practical methods of optimization*. John Wiley & Sons, 2000.

507 Yuchao Gu, Xintao Wang, Jay Zhangjie Wu, Yujun Shi, Yunpeng Chen, Zihan Fan, Wuyou Xiao, Rui Zhao,
508 Shuning Chang, Weijia Wu, et al. Mix-of-show: Decentralized low-rank adaptation for multi-concept
509 customization of diffusion models. In *Advances in Neural Information Processing Systems (NIPS)*, volume 36,
510 pages 15890–15902, 2023.

511 Vineet Gupta, Tomer Koren, and Yoram Singer. Shampoo: Preconditioned stochastic tensor optimization. In
512 *International Conference on Machine Learning (ICML)*, pages 1842–1850. PMLR, 2018.

513 Soufiane Hayou, Nikhil Ghosh, and Bin Yu. Lora+: Efficient low rank adaptation of large models. In
514 *International Conference on Machine Learning (ICML)*, pages 17783–17806. PMLR, 2024.

515 Jack Hessel, Ari Holtzman, Maxwell Forbes, Ronan Le Bras, and Yejin Choi. Clipscore: A reference-free
516 evaluation metric for image captioning. In *EMNLP (1)*, 2021.

517 Martin Heusel, Hubert Ramsauer, Thomas Unterthiner, Bernhard Nessler, and Sepp Hochreiter. Gans trained
518 by a two time-scale update rule converge to a local nash equilibrium. In *Advances in neural information
519 processing systems (NIPS)*, volume 30, 2017.

520 Edward J Hu, Yelong Shen, Phillip Wallis, Zeyuan Allen-Zhu, Yuanzhi Li, Shean Wang, Lu Wang, Weizhu
521 Chen, et al. Lora: Low-rank adaptation of large language models. In *International Conference on Learning
522 Representations (ICLR)*, volume 1, page 3, 2022.

523 Diederik P Kingma and Jimmy Ba. Adam: A method for stochastic optimization. *arXiv preprint arXiv:1412.6980*,
524 2014.

525 Yann LeCun, Léon Bottou, Genevieve B Orr, and Klaus-Robert Müller. Efficient backprop. In *Neural networks:
526 Tricks of the trade*, pages 9–50. Springer, 2002.

527 Aixin Liu, Bei Feng, Bing Xue, Bingxuan Wang, Bochao Wu, Chengda Lu, Chenggang Zhao, Chengqi Deng,
528 Chenyu Zhang, Chong Ruan, et al. Deepseek-v3 technical report. *arXiv preprint arXiv:2412.19437*, 2024a.

529 Shih-Yang Liu, Chien-Yi Wang, Hongxu Yin, Pavlo Molchanov, Yu-Chiang Frank Wang, Kwang-Ting Cheng,
530 and Min-Hung Chen. Dora: Weight-decomposed low-rank adaptation. In *International Conference on
531 Machine Learning (ICML)*, 2024b.

532 Yinhan Liu, Myle Ott, Naman Goyal, Jingfei Du, Mandar Joshi, Danqi Chen, Omer Levy, Mike Lewis, Luke
533 Zettlemoyer, and Veselin Stoyanov. Roberta: A robustly optimized bert pretraining approach. *arXiv preprint*
534 *arXiv:1907.11692*, 2019.

540 Ilya Loshchilov and Frank Hutter. Decoupled weight decay regularization. *arXiv preprint arXiv:1711.05101*,
 541 2017.

542 CS Lu. Solution of the matrix equation $ax+xb=c$. *Electronics Letters*, 7(8):185–186, 1971.

544 James Martens and Roger Grosse. Optimizing neural networks with kronecker-factored approximate curvature.
 545 In *International conference on machine learning (ICML)*, pages 2408–2417. PMLR, 2015.

546 Zhanfeng Mo, Long-Kai Huang, and Sinno Jialin Pan. Parameter and memory efficient pretraining via low-rank
 547 riemannian optimization. In *International Conference on Learning Representations (ICLR)*, 2025.

549 Depen Morwani, Itai Shapira, Nikhil Vyas, Sham M Kakade, Lucas Janson, et al. A new perspective on
 550 shampoo’s preconditioner. In *International Conference on Learning Representations (ICLR)*, 2024.

551 Linyong Nan, Dragomir Radev, Rui Zhang, Amrit Rau, Abhinand Sivaprasad, Chiachun Hsieh, Xiangru Tang,
 552 Aadit Vyas, Neha Verma, Pranav Krishna, et al. Dart: Open-domain structured data record to text generation.
 553 In *Proceedings of the 2021 Conference of the North American Chapter of the Association for Computational
 554 Linguistics: Human Language Technologies*, pages 432–447, 2021.

555 Jorge Nocedal and Stephen J Wright. *Numerical optimization*. Springer, 2006.

556 Jekaterina Novikova, Ondřej Dušek, and Verena Rieser. The e2e dataset: New challenges for end-to-end
 557 generation. *arXiv preprint arXiv:1706.09254*, 2017.

559 Adam Paszke, Sam Gross, Francisco Massa, Adam Lerer, James Bradbury, Gregory Chanan, Trevor Killeen,
 560 Zeming Lin, Natalia Gimelshein, Luca Antiga, et al. Pytorch: An imperative style, high-performance deep
 561 learning library. In *Advances in neural information processing systems (NIPS)*, volume 32, 2019.

562 Alec Radford, Jeffrey Wu, Rewon Child, David Luan, Dario Amodei, Ilya Sutskever, et al. Language models are
 563 unsupervised multitask learners. *OpenAI blog*, 1(8):9, 2019.

564 Alec Radford, Jong Wook Kim, Chris Hallacy, Aditya Ramesh, Gabriel Goh, Sandhini Agarwal, Girish Sastry,
 565 Amanda Askell, Pamela Mishkin, Jack Clark, et al. Learning transferable visual models from natural language
 566 supervision. In *International conference on machine learning (ICML)*, pages 8748–8763. PMLR, 2021.

567 Noam Shazeer and Mitchell Stern. Adafactor: Adaptive learning rates with sublinear memory cost. In
 568 *International Conference on Machine Learning (ICML)*, pages 4596–4604. PMLR, 2018.

570 Tian Tong, Cong Ma, and Yuejie Chi. Accelerating ill-conditioned low-rank matrix estimation via scaled gradient
 571 descent. *Journal of Machine Learning Research*, 22(150):1–63, 2021.

572 Nikhil Vyas, Depen Morwani, Rosie Zhao, Itai Shapira, David Brandfonbrener, Lucas Janson, and Sham M
 573 Kakade. Soap: Improving and stabilizing shampoo using adam for language modeling. In *International
 574 Conference on Learning Representations (ICLR)*, 2025.

575 Shaowen Wang, Linxi Yu, and Jian Li. Lora-ga: Low-rank adaptation with gradient approximation. In *Advances
 576 in Neural Information Processing Systems (NIPS)*, volume 37, pages 54905–54931, 2024.

577 Zhengbo Wang, Jian Liang, Ran He, Zilei Wang, and Tieniu Tan. Lora-pro: Are low-rank adapters properly
 578 optimized? In *International Conference on Learning Representations (ICLR)*, 2025.

580 Ke Wei, Jian-Feng Cai, Tony F Chan, and Shingyu Leung. Guarantees of riemannian optimization for low rank
 581 matrix recovery. *SIAM Journal on Matrix Analysis and Applications*, 37(3):1198–1222, 2016.

582 An Yang, Baosong Yang, Beichen Zhang, Binyuan Hui, Bo Zheng, Bowen Yu, Chengyuan Li, Dayiheng Liu,
 583 Fei Huang, Haoran Wei, et al. Qwen2.5 technical report. *arXiv preprint arXiv:2412.15115*, 2024.

584 Jui-Nan Yen, Si Si, Zhao Meng, Felix Yu, Sai Surya Duvvuri, Inderjit S Dhillon, Cho-Jui Hsieh, and Sanjiv
 585 Kumar. Lora done rite: Robust invariant transformation equilibration for lora optimization. In *The Thirteenth
 586 International Conference on Learning Representations*.

587 Fangzhao Zhang and Mert Pilanci. Riemannian preconditioned lora for fine-tuning foundation models. In
 588 *International Conference on Machine Learning (ICML)*, 2024.

590 Yilang Zhang, Bingcong Li, and Georgios B Giannakis. Reflora: Refactored low-rank adaptation for efficient
 591 fine-tuning of large models. *arXiv preprint arXiv:2505.18877*, 2025a.

592 Yuanhe Zhang, Fanghui Liu, and Yudong Chen. Lora-one: One-step full gradient could suffice for fine-tuning
 593 large language models, provably and efficiently. In *International Conference on Machine Learning (ICML)*,
 2025b.

594 Jiawei Zhao, Zhenyu Zhang, Beidi Chen, Zhangyang Wang, Anima Anandkumar, and Yuandong Tian. Galore:
595 Memory-efficient llm training by gradient low-rank projection. In *International Conference on Machine*
596 *Learning (ICML)*, pages 61121–61143. PMLR, 2024.

597 Zhenyu Zhu, Yongtao Wu, Quanquan Gu, and Volkan Cevher. Imbalance-regularized lora: A plug-and-play
598 method for improving fine-tuning of foundation models. In *Adaptive Foundation Models: Evolving AI for*
599 *Personalized and Efficient Learning*, 2024.

600

601

602

603

604

605

606

607

608

609

610

611

612

613

614

615

616

617

618

619

620

621

622

623

624

625

626

627

628

629

630

631

632

633

634

635

636

637

638

639

640

641

642

643

644

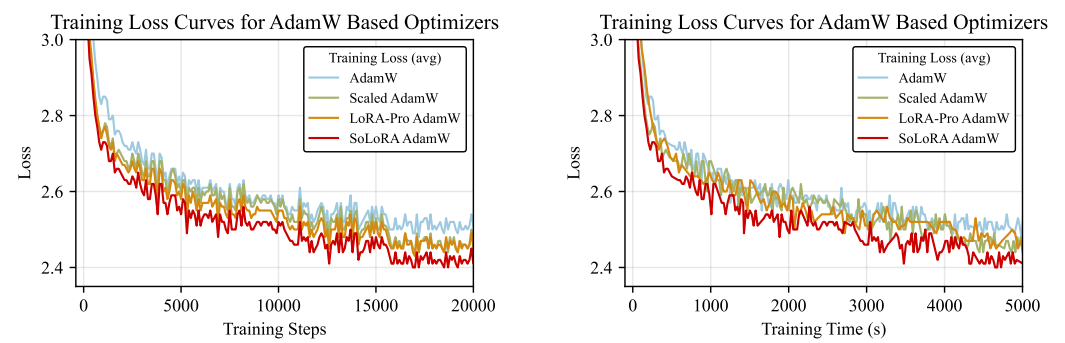
645

646

647

648	CONTENTS																																																							
649																																																								
650	A Supplementary Experiments of GPT-2 Fine-tuning	13																																																						
651	A.1 Experimental Results For Different Datasets	13																																																						
652	A.2 Experimental Results For Different Model Size	13																																																						
653	A.3 Training Loss Curve Using Different Optimizers	14																																																						
654	A.4 Training Efficiency Comparison	14																																																						
655	A.5 Parameter Settings	15																																																						
656																																																								
657	B Supplementary Experiments of Diffusion Model Fine-tuning	17																																																						
658	B.1 Evaluation Metrics of Diffusion Models	18																																																						
659	B.2 Experimental Results for Different LoRA Scaling Factors	18																																																						
660	B.3 Experimental Results for Different Learning Rates	19																																																						
661																																																								
662	C Computational and Memory Complexity Analysis of SoLoRA	24																																																						
663																																																								
664	D Proof of Theoretical Results	24																																																						
665	D.1 Computation of Jacobian	24																																																						
666	D.2 Orthogonal Projection to Tangent Space	25																																																						
667	D.3 Proofs of Theorem 3.1 and Theorem 3.2	27																																																						
668	D.4 Proof of the loss function exhibits a decreasing trend	28																																																						
669																																																								
670	E Additional Experiments	30																																																						
671																																																								
672	F The Use of Large Language Models (LLMs)	30																																																						
673																																																								
674	A SUPPLEMENTARY EXPERIMENTS OF GPT-2 FINE-TUNING																																																							
675																																																								
676																																																								
677																																																								
678	A.1 EXPERIMENTAL RESULTS FOR DIFFERENT DATASETS																																																							
679																																																								
680	To further validate the effectiveness of SoLoRA, we also conducted the experiments of GPT-2																																																							
681	fine-tuning on the DART (Nan et al., 2021) dataset. with the results provided in the following table.																																																							
682																																																								
683	Scores of GPT-2 small model (rank=4) fine-tuned using different optimizers. Evaluation is conducted																																																							
684	on DART dataset.																																																							
685																																																								
686	<table border="1"> <thead> <tr> <th>Methods</th> <th>BLEU\uparrow</th> <th>METEOR\uparrow</th> <th>chrF++\uparrow</th> <th>TER\downarrow</th> <th>BLEURT\uparrow</th> </tr> </thead> <tbody> <tr> <td>SGD</td> <td>41.2</td> <td>0.63</td> <td>0.59</td> <td>0.52</td> <td>0.33</td> </tr> <tr> <td>Scaled GD</td> <td>43.8</td> <td>0.66</td> <td>0.61</td> <td>0.50</td> <td>0.38</td> </tr> <tr> <td>LoRA-Pro SGD</td> <td>44.1</td> <td>0.66</td> <td>0.61</td> <td>0.50</td> <td>0.38</td> </tr> <tr> <td>SoLoRA SGD (ours)</td> <td>44.6</td> <td>0.66</td> <td>0.62</td> <td>0.49</td> <td>0.39</td> </tr> <tr> <td>AdamW</td> <td>43.9</td> <td>0.66</td> <td>0.60</td> <td>0.50</td> <td>0.38</td> </tr> <tr> <td>Scaled AdamW</td> <td>44.8</td> <td>0.67</td> <td>0.62</td> <td>0.49</td> <td>0.40</td> </tr> <tr> <td>LoRA-Pro AdamW</td> <td>44.9</td> <td>0.66</td> <td>0.62</td> <td>0.50</td> <td>0.39</td> </tr> <tr> <td>SoLoRA AdamW (ours)</td> <td>45.4</td> <td>0.67</td> <td>0.60</td> <td>0.49</td> <td>0.40</td> </tr> </tbody> </table>	Methods	BLEU \uparrow	METEOR \uparrow	chrF++ \uparrow	TER \downarrow	BLEURT \uparrow	SGD	41.2	0.63	0.59	0.52	0.33	Scaled GD	43.8	0.66	0.61	0.50	0.38	LoRA-Pro SGD	44.1	0.66	0.61	0.50	0.38	SoLoRA SGD (ours)	44.6	0.66	0.62	0.49	0.39	AdamW	43.9	0.66	0.60	0.50	0.38	Scaled AdamW	44.8	0.67	0.62	0.49	0.40	LoRA-Pro AdamW	44.9	0.66	0.62	0.50	0.39	SoLoRA AdamW (ours)	45.4	0.67	0.60	0.49	0.40	
Methods	BLEU \uparrow	METEOR \uparrow	chrF++ \uparrow	TER \downarrow	BLEURT \uparrow																																																			
SGD	41.2	0.63	0.59	0.52	0.33																																																			
Scaled GD	43.8	0.66	0.61	0.50	0.38																																																			
LoRA-Pro SGD	44.1	0.66	0.61	0.50	0.38																																																			
SoLoRA SGD (ours)	44.6	0.66	0.62	0.49	0.39																																																			
AdamW	43.9	0.66	0.60	0.50	0.38																																																			
Scaled AdamW	44.8	0.67	0.62	0.49	0.40																																																			
LoRA-Pro AdamW	44.9	0.66	0.62	0.50	0.39																																																			
SoLoRA AdamW (ours)	45.4	0.67	0.60	0.49	0.40																																																			
687																																																								
688																																																								
689																																																								
690																																																								
691																																																								
692																																																								
693																																																								
694																																																								
695																																																								
696																																																								
697	A.2 EXPERIMENTAL RESULTS FOR DIFFERENT MODEL SIZE																																																							
698																																																								
699	To more comprehensively validate the advantages of SoLoRA, we conduct experiments not only on																																																							
700	the small GPT-2 model but also on GPT-2 models of varying sizes for broader evaluation. All models																																																							
701	are fine-tuned with rank 4, and the evaluation results are presented in Table 2. The specific parameter																																																							
	settings can be found in Table 3 and Table 4. By testing on models of different sizes, the experimental																																																							

702 results clearly demonstrate that SoLoRA significantly outperforms other algorithms, regardless of
 703 whether the SGD optimizer or the AdamW optimizer is used. This further confirms the effectiveness
 704 and stability of the SoLoRA algorithm, enabling it to maintain excellent performance across models
 705 of different sizes and under different optimizers.



718 (a) Training loss curve over training steps when fine-
 719 tuning using AdamW-based method.
 720 (b) Training loss curve over training time when fine-
 721 tuning using AdamW-based method.

721 Figure 2: Training loss of GPT-2 small model ($r = 64$) fine-tuned using different AdamW-based
 722 optimizers. Evaluation is conducted on E2E Natural Language Generation Challenge.

725 A.3 TRAINING LOSS CURVE USING DIFFERENT OPTIMIZERS

727 To further explore the performance advantages of SoLoRA, we compare the runtime of different
 728 optimizers when fine-tuning large language models, with the results shown in Figures 1 and 2.
 729 These results strongly demonstrate the significant efficiency improvements achieved by the SoLoRA
 730 method in fine-tuning tasks. Additionally, Figure 3 illustrates the stability of SoLoRA under different
 731 learning rates. The experimental results show that SoLoRA maintains stable performance across
 732 a wide range of learning rates, which is crucial for parameter tuning in practical applications. To
 733 more comprehensively evaluate the stability of SoLoRA, we also compare it with Scaled AdamW
 734 and LoRA-Pro AdamW, under varying learning rates. The results are presented in Figure 3. The
 735 comparison reveals that SoLoRA exhibits superior stability across different ranks and learning rates.
 736 This indicates that SoLoRA is not only insensitive to changes in learning rates but also robust across
 737 varying LoRA ranks. As a result, it reduces the difficulty of hyperparameter tuning and enhances its
 738 practicality in fine-tuning.

740 A.4 TRAINING EFFICIENCY COMPARISON

742 To validate the training and inference efficiency of SoLoRA, we report in the table below the total
 743 training time required for all algorithms on the GPT-2 small model (rank 64). In addition, we recorded
 744 the relationship between training time and the number of steps in Figure 4.

746 Training and Inference Time of GPT-2 small model (rank=64) fine-tuned using different optimizers.
 747 Evaluation is conducted on E2E dataset.

Methods	SGD	Scaled GD	LoRA-Pro SGD	SoLoRA SGD
Total Training Time (Hours)	1.79	1.92	2.78	2.04
Total Inference Time (Hours)	1.86	1.87	1.58	1.89
Methods	AdamW	Scaled AdamW	LoRA-Pro AdamW	SoLoRA AdamW
Total Training Time (Hours)	1.79	1.94	2.93	2.04
Total Inference Time (Hours)	1.87	1.88	1.89	1.86

To further validate this, we record GPU memory consumption when the optimizer is called and after the backward is called (fine-tune GPT-2 small model with rank as 4). The results are summarized below.

GPU Memory occupied of GPT-2 small model (rank=4) fine-tuned using different optimizers. Evaluation is conducted on E2E dataset.

Methods	SGD	Scaled GD	LoRA-Pro SGD	SoLoRA SGD
During optimizer computation (MB)	1395.48	1395.57	1395.62	1401.01
After backward (MB)	1395.48	1395.48	1395.48	1395.62
Memory Complexity	0	0	0	$m+n$
Methods	AdamW	Scaled AdamW	LoRA-Pro AdamW	SoLoRA AdamW
During optimizer computation (MB)	1396.63	1396.72	1529.97	1462.51
After backward (MB)	1396.60	1396.60	1510.98	1457.12
Memory Complexity	$(m+n)r$	$(m+n)r$	$2mn$	$mn+m+n$

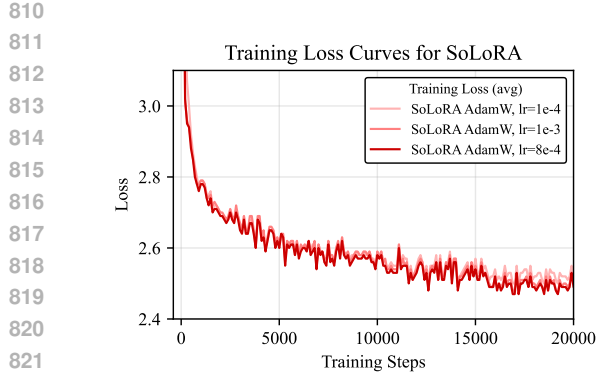
The results confirm that the memory usage of Algorithm 1 is comparable to other algorithms. Specifically, SoLoRA SGD (Algorithm 1) increases memory usage by only $(1401.01-1395.62)/1395.62 = 0.386\%$ compared to LoRA-SGD. However, with this slight increase in memory, Algorithm 1 demonstrates an effective improvement, as shown in Table 2.

Table 2: Scores of GPT-2 small and medium models ($r = 4$) fine-tuned using different optimizers. Evaluation is conducted on E2E Natural Language Generation challenge. See Appendix A.2 for experimental details.

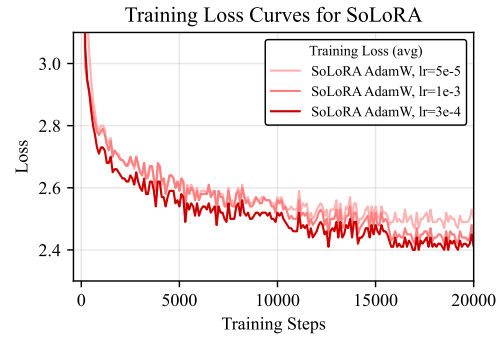
Model	Method	E2E				
		BLEU	NIST	MET	ROUGE-L	CIDEr
GPT-2 small	SGD	54.8	4.56	34.0	63.3	1.29
	Scaled GD	68.5	8.72	45.5	69.4	2.40
	LoRA-Pro SGD	68.4	8.72	45.5	69.6	2.43
	SoLoRA SGD (ours)	69.5	8.77	46.5	71.5	2.50
GPT-2 medium	AdamW	69.1	8.75	46.0	70.5	2.47
	Scaled AdamW	69.5	8.80	46.2	70.9	2.48
	LoRA-Pro AdamW	69.2	8.73	45.9	70.8	2.47
	SoLoRA AdamW (ours)	70.0	8.84	46.3	71.3	2.50
	SGD	66.6	8.54	44.2	68.2	2.32
	Scaled GD	69.2	8.71	46.3	70.9	2.48
	LoRA-Pro SGD	69.7	8.77	46.5	70.9	2.50
	SoLoRA SGD (ours)	70.3	8.84	46.9	71.7	2.54
	AdamW	68.9	8.69	46.5	71.3	2.51
	Scaled AdamW	69.6	8.77	46.6	71.8	2.52
	LoRA-Pro AdamW	69.8	8.78	46.5	71.7	2.52
	SoLoRA AdamW (ours)	70.3	8.84	46.7	71.8	2.53

A.5 PARAMETER SETTINGS

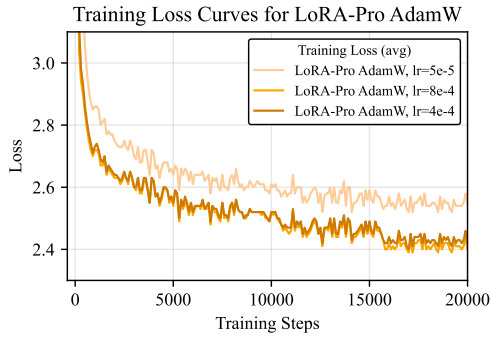
To ensure the reproducibility of the experiments described in Section 4 and to facilitate verification and comparison by others, we provide the complete details of the experimental parameter settings. Tables 3 and 4 list the parameters used during the fine-tuning of GPT-2 models and the learning rates corresponding to different optimizers, respectively. Specifically, we conduct experiments with GPT-2 models of various sizes. “Rank 4 (M)” represents a medium-sized model using LoRA with rank 4, while “Rank 4”, “Rank 16”, and “Rank 64” represent small models using LoRA with ranks 4, 16, and 64, respectively. To ensure the fairness of the experimental setup, we follow the parameter settings in LoRA (Hu et al., 2022) and Riemannian Preconditioned LoRA (Zhang and Pilanci, 2024). However,



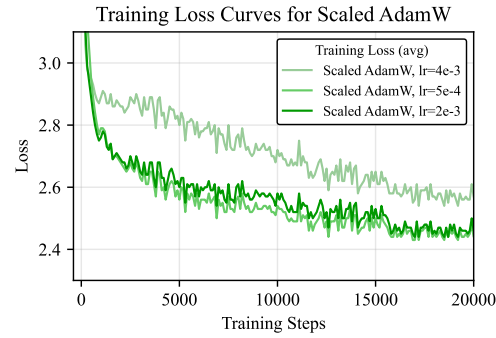
(a) Training loss curve over training step when fine-tuning using SoLoRA AdamW with different learning rates. LoRA rank is 16, with 8e-4 being the optimal learning rate.



(b) Training loss curve over training step when fine-tuning using SoLoRA AdamW with different learning rates. LoRA rank is 64, with 3e-4 being the best learning rate.

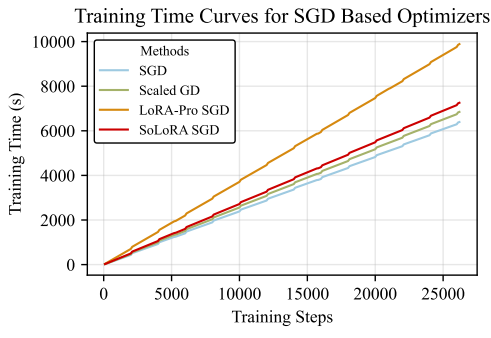


(c) Training loss curve over training step when fine-tuning using LoRA-Pro AdamW with different learning rates. LoRA rank is 64, with 4e-4 being the best learning rate.

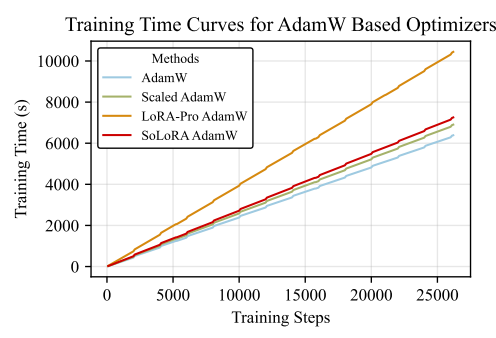


(d) Training loss curve over training step when fine-tuning using Scaled AdamW with different learning rates. LoRA rank is 64, with 2e-3 being the best learning rate.

Figure 3: Training loss curve over training step of GPT-2 small model ($r = 16$ and 64) fine-tuned using different learning rates. Evaluation is conducted on E2E Natural Language Generation Challenge. Our optimizer is stable across different learning rates under varying ranks.



(a) Training Time curve over training steps when fine-tuning using SGD-based method.



(b) Training Time curve over training steps when fine-tuning using AdamW-based method.

Figure 4: Training Time of GPT-2 small model ($r = 64$) fine-tuned using different optimizers. Evaluation is conducted on E2E Natural Language Generation Challenge.

864
 865
 866
 867
 868
 869
 870
 871
 872
 873
 874
 875
 876
 877
 878
 879
 880
 881
 882
 883
 884
 885
 886
 887
 888
 889
 890
 891
 892
 893
 894
 895
 896
 897
 898
 899
 900
 901
 902
 903
 904
 905
 906
 907
 908
 909
 910
 911
 912
 913
 914
 915
 916
 917
 918
 919
 920
 921
 922
 923
 924
 925
 926
 927
 928
 929
 930
 931
 932
 933
 934
 935
 936
 937
 938
 939
 940
 941
 942
 943
 944
 945
 946
 947
 948
 949
 950
 951
 952
 953
 954
 955
 956
 957
 958
 959
 960
 961
 962
 963
 964
 965
 966
 967
 968
 969
 970
 971
 972
 973
 974
 975
 976
 977
 978
 979
 980
 981
 982
 983
 984
 985
 986
 987
 988
 989
 990
 991
 992
 993
 994
 995
 996
 997
 998
 999
 9999

considering the sensitivity of different optimizers to learning rates, we use a grid search strategy to independently tune the optimal learning rate for each optimizer. This ensures that each optimizer operates under its best-performing configuration, providing more objective and reliable experimental results.

Table 3: Training and Inference Configuration for GPT-2 Fine-tuning.

Training	LoRA α		Inference		
Parameter	Value	Parameter	Value	Parameter	Value
Dropout Probability	0.1				
Batch Size	8				
Number of Epochs	5	α (for Rank 4)	32	Beam Size	10
Warm-up Steps	500	α (for Rank 16)	32	Length Penalty	0.8
Learning Rate Scheduler	Linear	α (for Rank 64)	128	No Repeat Ngram Size	4
Label Smoothing	0.1				
Weight Decay	0.01				

Table 4: Core Optimizer Parameters for GPT-2 fine-tuning.

Methods	Learning Rate ($\times 10^{-3}$)					β_3	$\beta_1 = \beta_2$
	Rank 4	Rank 4 (M)	Rank 16	Rank 64			
SGD	90	90	200	90	/	/	
Scaled GD	20	20	40	10	/	/	
LoRA-Pro SGD	40	40	40	40	/	/	
SoLoRA SGD	0.05	0.05	0.5	0.8	/	0.98	
AdamW	0.2	0.2	0.2	0.2	0.9	0.999	
Scaled AdamW	0.8	0.8	2	4	0.7	0.8	
LoRA-Pro AdamW	0.1	0.1	0.2	0.4	0.9	0.999	
SoLoRA AdamW	0.5	0.1	0.8	0.3	0.9	0.98	

B SUPPLEMENTARY EXPERIMENTS OF DIFFUSION MODEL FINE-TUNING

As diffusion models increasingly become the mainstream method in image generation, LoRA plays an indispensable role in personalization and style transfer for specific characters. It demonstrates unique advantages, particularly in terms of parameter efficiency, training stability, and rapid convergence. To systematically evaluate the effectiveness of our optimizer SoLoRA in such personalized generation scenarios, we conduct experiments using the Mix-of-Show framework (Gu et al., 2023). This framework integrates Embedding Decomposed LoRA (EDLoRA) into the model, which further reduces the number of trainable parameters while maintaining expressive power. This design better aligns with the dual demands of computational efficiency and generalization stability in real-world applications. To ensure reproducibility and fair comparison, we follow the training and inference settings from (Zhang and Pilanci, 2024; Gu et al., 2023). Specifically, we disable fine-tuning of all embedding vectors and only fine-tune LoRA-related components of the text encoder and U-Net submodules.

Our evaluation encompasses two main aspects: quantitative assessment of the generated images based on objective metrics, as detailed in Section B.1, and qualitative demonstrations of the generated images to visually showcase the effectiveness of the optimizer. For qualitative evaluation, we use examples of Harry Potter and Hermione Granger to visually compare the performance of different optimizers in terms of identity preservation, scene conformity with prompt, and style diversity. As shown in Section B.2 and Section B.3, we conduct image generation under different LoRA scaling factors and compare the performance of various optimizers across multiple learning rates. This design not only evaluates the robustness of the optimizers under multi-scale hyperparameters but also reflects their overall impact on generation quality and consistency in real-world scenarios.

918 All experimental results consistently demonstrate the advantages of the SoLoRA algorithm. Both
 919 the quantitative evaluation metrics and the qualitative image demonstrations highlight the superior
 920 performance of SoLoRA. This success can be attributed to the ability of SoLoRA to effectively
 921 leverage the second-order information of the loss function, enabling more precise updates to model
 922 parameters. Furthermore, the low-rank approximations of gradients derived from our proposed
 923 adaptive weighted gradient strategy bring the performance of low-rank fine-tuning closer to that of
 924 full-parameter fine-tuning. This allows SoLoRA to achieve comparable performance to full-parameter
 925 fine-tuning while significantly reducing computational costs.

927 B.1 EVALUATION METRICS OF DIFFUSION MODELS

929 For quantitative evaluation, we employ two metrics: CLIP score (Hessel et al., 2021) and FID
 930 (Heusel et al., 2017). The CLIP score, based on the ViT-B/32 variant of the CLIP model (Radford
 931 et al., 2021), measures the consistency between the generated images and the input text prompts. The
 932 score ranges from 0 to 100, with higher scores indicating better alignment between the generated
 933 image and the text prompt. On the other hand, FID assesses the similarity between the distribution of
 934 generated images and the reference images. Lower FID values indicate higher similarity and better
 935 overall image quality. The experimental results are shown in Table 5.

936 In terms of FID, regardless of whether the SGD or AdamW optimizer is used, or whether the scaling
 937 factor is 0.7 or 1, our algorithm consistently achieve significantly lower FID values compared to all
 938 other methods. This strongly indicates that the distribution of images generated by our algorithm
 939 closely matches the distribution of the reference images. For the CLIP score, our algorithm achieve
 940 the best performance when the scaling factor is set to 1, outperforming all other methods. However,
 941 when the scaling factor is 0.7, the CLIP score of our algorithm is comparable to those of LoRA-Pro
 942 and AdamW algorithm. It is important to note that this does not imply that the quality of the images
 943 generated by our algorithm is inferior to others. On the contrary, this highlights one of the key
 944 strengths of our algorithm: by effectively leveraging second-order information from the loss function,
 945 the images generated by our method SoLoRA, not only maintain strong relevance to the text prompt
 946 but also exhibit richer details and greater diversity. For instance, in Figure 7, the clothing worn by
 947 the generated Harry Potter characters is more diverse, incorporating features that go beyond the
 948 simple text prompt. Similarly, in Figure 9, in addition to generating Harry Potter wearing a brown
 949 hat, our algorithm introduces more varied gestures for Harry Potter. These richer and more diverse
 950 features, while potentially causing a slight decrease in the CLIP score (as CLIP tends to prioritize
 951 strict prompt-image alignment and might not fully reward additional details beyond the prompt),
 952 actually enhance the overall quality and creativity of the generated images.

953 Table 5: CLIP and FID scores of different optimizers with different scaling factors for Mix-of>Show.

955 Methods	956 scaling=0.7		957 scaling=1	
	958 CLIP↑	959 FID↓	960 CLIP↑	961 FID↓
962 SGD	27.79	69.90	31.40	40.95
963 Scaled GD	31.23	35.86	30.60	29.62
964 LoRA-Pro SGD	31.47	34.30	30.48	29.19
965 SoLoRA SGD (ours)	31.47	30.17	31.58	28.18
966 AdamW	31.47	34.15	30.68	27.80
967 Scaled AdamW	24.21	48.23	24.51	34.18
968 LoRA-Pro AdamW	31.04	29.18	30.60	28.18
969 SoLoRA AdamW (ours)	31.47	29.01	30.73	27.13

968 B.2 EXPERIMENTAL RESULTS FOR DIFFERENT LORA SCALING FACTORS

970 To validate the effectiveness of the proposed optimizer, we compared the generated images of models
 971 trained using each optimizer under different LoRA scaling factors s . For the sake of fairness, we
 972 employed the optimal parameters for each optimizer, detailed in Table 6 for ease of replication.

972
 973
 974
 975
 976
 977
 978
 979
 980
 981
 982
 983
 984
 985
 986
 987
 988
 989
 990
 991
 992
 993
 994
 995
 996
 997
 998
 999
 1000
 1001
 1002
 1003
 1004
 1005
 1006
 1007
 1008
 1009
 1010
 1011
 1012
 1013
 1014
 1015
 1016
 1017
 1018
 1019
 1020
 1021
 1022
 1023
 1024
 1025

Figure 5 and 6 show the generated results for Harry Potter and Hermione Granger when fine-tuning the model using different AdamW-based optimizers, with the scaling factor set to 1.0. Figure 7 and 8 show the model’s generated results when fine-tuned using different SGD-based optimizers, with scaling factors uniformly set to 1.0. Figure 9 and 10 present the generated results by using different AdamW-based optimizers, employing the scaling factor of 0.7. Experimental results demonstrate that the models trained with our optimizer generate high-quality images, accurately reproducing the identity of Harry Potter and Hermione Granger while demonstrating diverse scene layouts adhering to the input prompts.

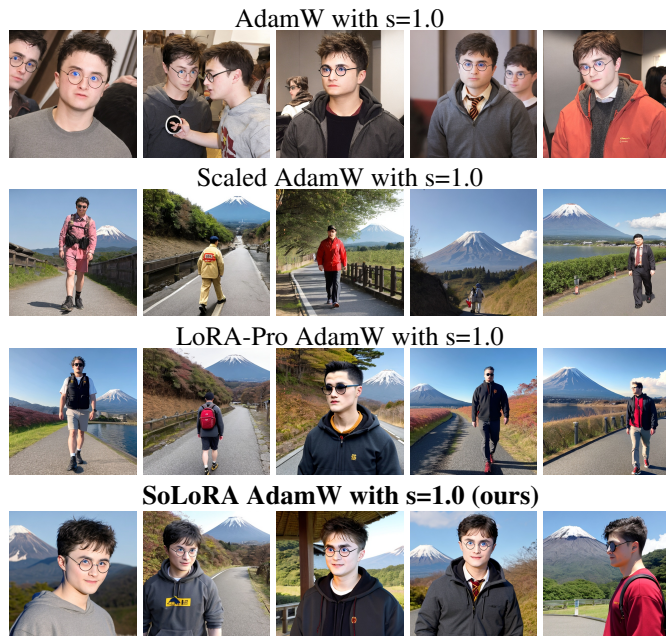


Figure 5: Generated results based on the prompt “Harry Potter is walking near Mount Fuji” when fine-tuned using AdamW-based optimizers. All optimizers employed a LoRA scaling factor of 1.0, with the best learning rate. The results indicate that the output of the model trained with our optimizer incorporates the character “Harry Potter”, the action “walking”, and the scene “Mount Fuji”, yielding superior image quality compared to alternative approaches.

B.3 EXPERIMENTAL RESULTS FOR DIFFERENT LEARNING RATES

To illustrate the stability of the proposed optimizer, we fix the scaling factor to 1.0 and conduct experiments for each optimizer when using different learning rates. For AdamW-based optimizers, we set AdamW to employ the “Small LR” learning rate combination of 5e-6 and 5e-5 for text-encoder and U-Net, and the “Large LR” learning rate combination of 1e-5 and 1e-4. For Scaled AdamW, LoRA-Pro AdamW, and SoLoRA AdamW, we employed the same learning rate combinations, the “Small LR” of 5e-6 and 5e-6, and the “Large LR” combination of 1e-5 and 1e-5. For SGD-based optimizers, SGD, Scaled GD, and LoRA-Pro SGD, we employ the “Small LR” combination of 1e-2 and 1e-2, and the “Large LR” combination of 1e-1 and 1e-1, whereas SoLoRA SGD utilized the “Small LR” combination of 5e-6 and 5e-6, and the “Large LR” combination of 1e-5 and 1e-5.

The experimental results, presented in Figures 11 and 12, illustrate the effectiveness of our proposed optimizer across both small and large learning rates. This consistent performance signifies a higher degree of stability compared to the alternatives. Such stability is paramount when fine-tuning diffusion models, as their training is characterized by a non-stationary loss landscape. Therefore, the optimizer’s ability to remain effective under varying learning rates makes it a robust and advantageous choice for this application.

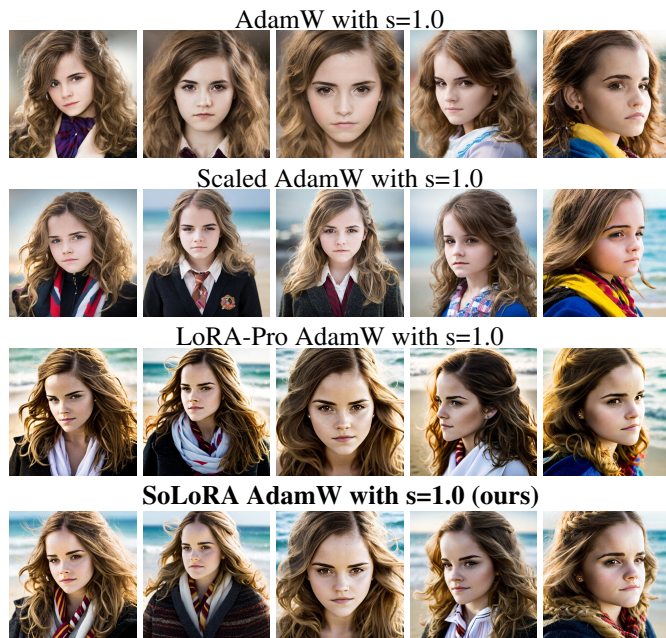


Figure 6: Generation results from the prompt “A photo of Hermione Granger on the beach, small waves, detailed symmetric face, beautiful composition” using AdamW-based optimizers. All the optimizers apply LoRA scaling factor as 1.0, with the best learning rate. Results demonstrate that the model trained with our optimizer generates higher-quality images than others, especially the face of Hermione Granger and the scene.



Figure 7: Generated results based on the prompt “Harry Potter standing near the lake” when fine-tuned using SGD-based optimizers. All optimizers employed a LoRA scaling factor of 1.0, with the best learning rate. Results demonstrate that the output images of the model trained with our optimizer have higher-quality than others, especially the face of Harry Potter.



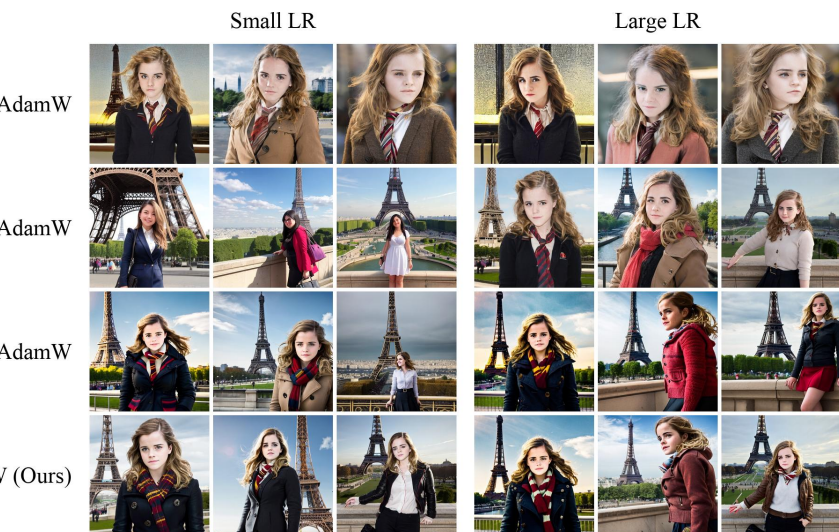
Figure 8: Generated results based on the prompt “Hermione Granger wearing a brown shirt” when fine-tuned using SGD-based optimizers. All optimizers employed a LoRA scaling factor of 1.0, with the best learning rate. Results demonstrate that the model trained with SoLoRA generates higher-quality images than others, especially the face of Hermione Granger.



Figure 9: Generated results based on the prompt “Harry Potter wearing a brown hat” when fine-tuned using AdamW-based optimizers. All optimizers employed a LoRA scaling factor of 0.7, with the best learning rate. The results indicate that the output of the model trained with SoLoRA incorporates the character “Harry Potter”, and the “hat”, yielding superior image quality compared to alternative approaches.



1156 Figure 10: Generation results from the prompt “A photo of Hermione Granger on the beach, small
 1157 waves, detailed symmetric face, beautiful composition” using AdamW-based optimizers. All the
 1158 optimizers apply LoRA scaling factor as 0.7. According to the author’s recommendation, the
 1159 optimizer AdamW and Scaled AdamW utilized a learning rate of 1e-5 for text-encoder and 1e-4 for
 1160 U-Net, whereas LoRA-Pro AdamW and our SoLoRA optimizer adopted 1e-5 for text-encoder and
 1161 U-Net. Results demonstrate that SoLoRA generates higher-quality images for both scaling factors
 1162 than others, including the face of Hermione Granger and the scene.



1184 Figure 11: Generated results based on the prompt “Hermione Granger in front of Eiffel Tower” using
 1185 AdamW-based optimizers. All the optimizers apply LoRA scaling factor as 1.0. “Small LR” and
 1186 “Large LR” represents using different learning rate, please refer to Appendix B.3 for more details.



Figure 12: Generated results based on the prompt “ Photo of Harry Potter” using SGD-based optimizers. All the optimizers apply LoRA scaling factor as 1.0. “Small LR” and “Large LR” represent using different learning rate, please refer to Appendix B.3 for more details.

Table 6: Optimizer Parameters for fine-tuning the Mix-of-Show Model.

Methods	Learning Rate Text-Encoder	Learning Rate U-Net	β_3	$\beta_1 = \beta_2$
SGD	1e-1	1e-1	/	/
Scaled GD	1e-1	1e-1	/	/
LoRA-Pro SGD	1e-1	1e-1	/	/
SoLoRA SGD	1e-5	1e-5	/	0.98
AdamW	1e-5	1e-4	0.9	0.999
Scaled AdamW	1e-5	1e-4	0.7	0.8
LoRA-Pro AdamW	1e-5	1e-5	0.9	0.999
SoLoRA AdamW	1e-5	1e-5	0.9	0.98

1242 **C COMPUTATIONAL AND MEMORY COMPLEXITY ANALYSIS OF SoLoRA**
 1243

1244 The update rule of SoLoRA is given by
 1245

$$\Delta_{\mathbf{A}_t} = (\mathbf{B}_t^\top \mathbf{L}_t^{\frac{1}{2}} \mathbf{B}_t)^{-1} \underbrace{\mathbf{B}_t^\top \mathbf{G}_t}_{\mathbf{G}_{\mathbf{A}_t}} \mathbf{R}_t^{-\frac{1}{2}} \left[\mathbf{I} - \frac{1}{2} \mathbf{R}_t^{\frac{1}{2}} \mathbf{A}_t^\top (\mathbf{A}_t \mathbf{R}_t^{\frac{1}{2}} \mathbf{A}_t^\top)^{-1} \mathbf{A}_t \right],$$

$$\Delta_{\mathbf{B}_t} = \left[\mathbf{I} - \frac{1}{2} \mathbf{B}_t (\mathbf{B}_t^\top \mathbf{L}_t^{\frac{1}{2}} \mathbf{B}_t)^{-1} \mathbf{B}_t^\top \mathbf{L}_t^{\frac{1}{2}} \right] \mathbf{L}_t^{-\frac{1}{2}} \underbrace{\mathbf{G}_t \mathbf{A}_t^\top}_{\mathbf{G}_{\mathbf{B}_t}} (\mathbf{A}_t \mathbf{R}_t^{\frac{1}{2}} \mathbf{A}_t^\top)^{-1}.$$

1246 We now analyze the computational complexity of computing the updates $\Delta_{\mathbf{A}_t}$ and $\Delta_{\mathbf{B}_t}$. For
 1247 simplicity, we focus on $\Delta_{\mathbf{A}_t}$, as the complexity for $\Delta_{\mathbf{B}_t}$ is symmetric.
 1248

- 1249 • Compute gradient \mathbf{G}_t . The stochastic gradient \mathbf{G}_t of \mathbf{W}_t is obtained during the backpropagation process.
 1250
- 1251 • Row and column sums for \mathbf{l}_t and \mathbf{r}_t . Compute \mathbf{l}_t and \mathbf{r}_t by summing the square of the element of \mathbf{G}_t along rows or columns, which is in the computation $\mathcal{O}(mn)$. $\mathbf{L}_t^{\frac{1}{2}}$ and $\mathbf{L}_t^{-\frac{1}{2}}$ can be computed in $\mathcal{O}(m)$, $\mathbf{R}_t^{\frac{1}{2}}$ and $\mathbf{R}_t^{-\frac{1}{2}}$ can be computed in $\mathcal{O}(n)$.
 1252
- 1253 • Compute $(\mathbf{B}_t^\top \mathbf{L}_t^{\frac{1}{2}} \mathbf{B}_t)^{-1} \mathbf{G}_{\mathbf{A}_t} \mathbf{R}_t^{-\frac{1}{2}}$. First to compute the inverse matrices $(\mathbf{B}_t^\top \mathbf{L}_t^{\frac{1}{2}} \mathbf{B}_t)^{-1}$ in $\mathcal{O}((m+r)r^2)$. Then multiply the inverse $(\mathbf{B}_t^\top \mathbf{L}_t^{\frac{1}{2}} \mathbf{B}_t)^{-1}$ by $\mathbf{G}_{\mathbf{A}_t}$ in $\mathcal{O}(nr^2)$, and multiply the diagonal matrix $\mathbf{R}_t^{-\frac{1}{2}}$ in $\mathcal{O}(nr)$.
 1254
- 1255 • Compute $(\mathbf{B}_t^\top \mathbf{L}_t^{\frac{1}{2}} \mathbf{B}_t)^{-1} \mathbf{G}_{\mathbf{A}_t} \mathbf{A}_t^\top (\mathbf{A}_t \mathbf{R}_t^{\frac{1}{2}} \mathbf{A}_t^\top)^{-1} \mathbf{A}_t$. First to compute the inverse matrices $(\mathbf{A}_t \mathbf{R}_t^{\frac{1}{2}} \mathbf{A}_t^\top)^{-1}$ in $\mathcal{O}((n+r)r^2)$. Use the result from the last step, multiply $(\mathbf{B}_t^\top \mathbf{L}_t^{\frac{1}{2}} \mathbf{B}_t)^{-1} \mathbf{G}_{\mathbf{A}_t}$ by \mathbf{A}_t^\top in computation $\mathcal{O}(nr^2)$, then multiply $(\mathbf{A}_t \mathbf{R}_t^{\frac{1}{2}} \mathbf{A}_t^\top)^{-1}$ in computation $\mathcal{O}(r^3)$, and multiply \mathbf{A}_t in $\mathcal{O}(nr^2)$.
 1256

1257 The computation complexity of $\Delta_{\mathbf{A}_t}$ is $\mathcal{O}(mn + (m+n)r^2 + r^3)$. The computation of $\Delta_{\mathbf{B}_t}$ follows
 1258 a similar structure, with symmetric terms. Its complexity is also $\mathcal{O}(mn + (m+n)r^2 + r^3)$. Then
 1259 we have
 1260

- 1261 • **Per Iteration Computational Complexity.** Combining the computations of $\Delta_{\mathbf{A}_t}$ and
 1262 $\Delta_{\mathbf{B}_t}$, the total computation complexity per iteration is $\mathcal{O}(mn + (m+n)r^2 + r^3)$.
 1263
- 1264 • **Memory Complexity.** The algorithm requires storing the vectors \mathbf{l}_t and \mathbf{r}_t in each iteration,
 1265 hence the memory complexity is $\mathcal{O}(m+n)$.
 1266

1267 **D PROOF OF THEORETICAL RESULTS**
 1268

1269 **D.1 COMPUTATION OF JACOBIAN**
 1270

1271 **Proposition D.1** (Computation of $J_{\mathcal{G}}$ and $J_{\mathcal{G}}^*$). *Let $[\mathbf{B}, \mathbf{A}]$ be a pair of low-rank factors with
 1272 $\mathbf{B} \in \mathbb{R}^{m \times r}, \mathbf{A} \in \mathbb{R}^{r \times n}$. Define the generator $\mathcal{G} : [\mathbb{R}^{m \times r}, \mathbb{R}^{r \times n}] \rightarrow \mathbb{R}^{m \times n}$ by $\mathcal{G}([\mathbf{B}, \mathbf{A}]) = \mathbf{B}\mathbf{A}$. Denote the Jacobian of \mathcal{G} by $J_{\mathcal{G}}$ and its adjoint by $J_{\mathcal{G}}^*$. Then, for any $[\mathbf{P}, \mathbf{Q}] \in [\mathbb{R}^{m \times r}, \mathbb{R}^{r \times n}]$ and
 1273 any $\mathbf{C} \in \mathbb{R}^{m \times n}$,*

- 1274 • $J_{\mathcal{G}}([\mathbf{B}, \mathbf{A}])[\mathbf{P}, \mathbf{Q}] = \mathbf{P}\mathbf{A} + \mathbf{B}\mathbf{Q}$,
 1275
- 1276 • $J_{\mathcal{G}}^*([\mathbf{B}, \mathbf{A}])(\mathbf{C}) = [\mathbf{C}\mathbf{A}^\top, \mathbf{B}^\top\mathbf{C}]$,
 1277
- 1278 • $J_{\mathcal{G}}([\mathbf{B}, \mathbf{A}])J_{\mathcal{G}}^*([\mathbf{B}, \mathbf{A}])(\mathbf{C}) = \mathbf{C}\mathbf{A}^\top\mathbf{A} + \mathbf{B}\mathbf{B}^\top\mathbf{C}$.
 1279

1280 *Proof.* The Jacobian operator $J_{\mathcal{G}}([\mathbf{B}, \mathbf{A}])[\mathbf{P}, \mathbf{Q}] : [\mathbb{R}^{m \times r}, \mathbb{R}^{r \times n}] \rightarrow \mathbb{R}^{m \times n}$ represents the derivative
 1281 of \mathcal{G} at $[\mathbf{B}, \mathbf{A}]$ along the direction $[\mathbf{P}, \mathbf{Q}]$. Similarly, $J_{\mathcal{G}}^*([\mathbf{B}, \mathbf{A}])(\mathbf{C}) : \mathbb{R}^{m \times n} \rightarrow [\mathbb{R}^{m \times r}, \mathbb{R}^{r \times n}]$
 1282 is the adjoint of $J_{\mathcal{G}}$ at $[\mathbf{B}, \mathbf{A}]$ along the direction \mathbf{C} . For more details, see (Absil et al., 2009,
 1283 Section 6.1).

1296 (i) The computation of $J_{\mathcal{G}}$. Let $\mathbf{B}(t) : \mathbb{R} \rightarrow \mathbb{R}^{m \times r}$ and $\mathbf{A}(t) : \mathbb{R} \rightarrow \mathbb{R}^{r \times n}$ be differentiable
 1297 curves with $\mathbf{B}(0) = \mathbf{B}$ and $\mathbf{A}(0) = \mathbf{A}$. By the chain rule, the Jacobian of \mathcal{G} at $[\mathbf{B}, \mathbf{A}]$
 1298 along these curves is

$$\begin{aligned} J_{\mathcal{G}}([\mathbf{B}(t), \mathbf{A}(t)])[\dot{\mathbf{B}}(t), \dot{\mathbf{A}}(t)] \Big|_{t=0} &= \left[\frac{d\mathcal{G}([\mathbf{B}, \mathbf{A}])}{d\mathbf{B}} \right] \dot{\mathbf{B}}(t) \Big|_{t=0} + \left[\frac{d\mathcal{G}([\mathbf{B}, \mathbf{A}])}{d\mathbf{A}} \right] \dot{\mathbf{A}}(t) \Big|_{t=0} \\ &= \dot{\mathbf{B}}(t)\mathbf{A}(t) \Big|_{t=0} + \mathbf{B}(t)\dot{\mathbf{A}}(t) \Big|_{t=0} \\ &= \dot{\mathbf{B}}(0)\mathbf{A} + \mathbf{B}\dot{\mathbf{A}}(0), \end{aligned}$$

1306 where $\dot{\mathbf{B}}(t)$ and $\dot{\mathbf{A}}(t)$ denote the derivatives of $\mathbf{B}(t)$ and $\mathbf{A}(t)$ with respect to t . The second
 1307 line follows because $\mathcal{G}([\mathbf{B}, \mathbf{A}]) = \mathbf{B}\mathbf{A}$, hence $\frac{d\mathcal{G}([\mathbf{B}, \mathbf{A}])}{d\mathbf{B}}$ and $\frac{d\mathcal{G}([\mathbf{B}, \mathbf{A}])}{d\mathbf{A}}$ are both linear
 1308 operators.

1309 Since $\dot{\mathbf{B}}(0)$ and $\dot{\mathbf{A}}(0)$ are arbitrary, for any $[\mathbf{P}, \mathbf{Q}] \in [\mathbb{R}^{m \times r}, \mathbb{R}^{r \times n}]$, we obtain

$$J_{\mathcal{G}}([\mathbf{B}, \mathbf{A}])[\mathbf{P}, \mathbf{Q}] = \mathbf{P}\mathbf{A} + \mathbf{B}\mathbf{Q}.$$

1312 (ii) The computation of $J_{\mathcal{G}}^*$. For brevity, write $J_{\mathcal{G}}[\mathbf{P}, \mathbf{Q}]$ for $J_{\mathcal{G}}([\mathbf{B}, \mathbf{A}])[\mathbf{P}, \mathbf{Q}]$ and $J_{\mathcal{G}}^*(\mathbf{C})$ for
 1313 $J_{\mathcal{G}}^*([\mathbf{B}, \mathbf{A}])(\mathbf{C})$. By definition of the adjoint (with respect to the Frobenius inner product),
 1314 for any $[\mathbf{P}, \mathbf{Q}] \in (\mathbb{R}^{m \times r}, \mathbb{R}^{r \times n})$ and $\mathbf{C} \in \mathbb{R}^{m \times n}$,

$$\langle J_{\mathcal{G}}[\mathbf{P}, \mathbf{Q}], \mathbf{C} \rangle = \langle [\mathbf{P}, \mathbf{Q}], J_{\mathcal{G}}^*(\mathbf{C}) \rangle.$$

1317 For the left-hand side,

$$\begin{aligned} \langle J_{\mathcal{G}}[\mathbf{P}, \mathbf{Q}], \mathbf{C} \rangle &= \langle \mathbf{P}\mathbf{A} + \mathbf{B}\mathbf{Q}, \mathbf{C} \rangle \\ &= \langle \mathbf{P}\mathbf{A}, \mathbf{C} \rangle + \langle \mathbf{B}\mathbf{Q}, \mathbf{C} \rangle \\ &= \langle \mathbf{P}, \mathbf{C}\mathbf{A}^\top \rangle + \langle \mathbf{Q}, \mathbf{B}^\top\mathbf{C} \rangle. \end{aligned}$$

1322 For the right-hand side, writing $J_{\mathcal{G}}^*(\mathbf{C}) = [\mathbf{C}_1, \mathbf{C}_2]$, then

$$\begin{aligned} \langle [\mathbf{P}, \mathbf{Q}], J_{\mathcal{G}}^*(\mathbf{C}) \rangle &= \langle [\mathbf{P}, \mathbf{Q}], [\mathbf{C}_1, \mathbf{C}_2] \rangle \\ &= \langle \mathbf{P}, \mathbf{C}_1 \rangle + \langle \mathbf{Q}, \mathbf{C}_2 \rangle. \end{aligned}$$

1326 Hence $\mathbf{C}_1 = \mathbf{C}\mathbf{A}^\top$ and $\mathbf{C}_2 = \mathbf{B}^\top\mathbf{C}$, and therefore $J_{\mathcal{G}}^*([\mathbf{B}, \mathbf{A}])(\mathbf{C}) = [\mathbf{C}\mathbf{A}^\top, \mathbf{B}^\top\mathbf{C}]$.

1328 (iii) Finally, $J_{\mathcal{G}}([\mathbf{B}, \mathbf{A}])J_{\mathcal{G}}^*([\mathbf{B}, \mathbf{A}])(\mathbf{C}) = J_{\mathcal{G}}([\mathbf{B}, \mathbf{A}])[\mathbf{C}\mathbf{A}^\top, \mathbf{B}^\top\mathbf{C}] = \mathbf{C}\mathbf{A}^\top\mathbf{A} + \mathbf{B}\mathbf{B}^\top\mathbf{C}$
 1329 as claimed.

1331 \square

1332 D.2 ORTHOGONAL PROJECTION TO TANGENT SPACE

1335 In this subsection, we derive the orthogonal projection onto the tangent space under both the standard
 1336 metric and the weighted metric. The specific forms of \mathbf{L}_t and \mathbf{R}_t are presented here and will not be
 1337 repeated in subsequent propositions and proofs. For the sake of simplicity, the subscript t will be
 1338 omitted in this subsection.

$$\begin{aligned} \mathbf{L}_t &= \text{diag}(\mathbf{l}_t / \sqrt{\|\mathbf{l}_t\|_1}) \text{ with } \mathbf{l}_t = \beta_2 \mathbf{l}_{t-1} + (1 - \beta_2) \sum_{j=1}^n (\mathbf{G}_t \odot \mathbf{G}_t)_{i,j}, \\ \mathbf{R}_t &= \text{diag}(\mathbf{r}_t / \sqrt{\|\mathbf{r}_t\|_1}) \text{ with } \mathbf{r}_t = \beta_3 \mathbf{r}_{t-1} + (1 - \beta_3) \sum_{i=1}^m (\mathbf{G}_t \odot \mathbf{G}_t)_{i,j}, \end{aligned} \tag{13}$$

1344 where \odot denotes the Hadamard (elementwise) product and $\mathbf{G}_t = \nabla \mathcal{L}(\mathbf{W}_0 + \mathbf{W}_t)$.

1345 **Proposition D.2** (Orthogonal Projection to Tangent Space Under the Standard Metric). *Let $\mathbf{W} \in \mathcal{M}_r$
 1346 be a rank- r matrix with a low-rank decomposition $\mathbf{W} = \mathbf{B}\mathbf{A}$, where $\mathbf{B} \in \mathbb{R}^{m \times r}$, $\mathbf{A} \in \mathbb{R}^{r \times n}$. Denote
 1347 by $\mathbb{T}_{\mathbf{W}}$ the tangent space of the smooth manifold \mathcal{M}_r at the point \mathbf{W} . Then, the orthogonal projection
 1348 of any matrix $\mathbf{Z} \in \mathbb{R}^{m \times n}$ onto $\mathbb{T}_{\mathbf{W}}$ is given by*

$$\mathcal{P}_{\mathbb{T}_{\mathbf{W}}}(\mathbf{Z}) = \mathbf{B}(\mathbf{B}^\top\mathbf{B})^{-1}\mathbf{B}^\top\mathbf{Z} + \mathbf{Z}\mathbf{A}^\top(\mathbf{A}\mathbf{A}^\top)^{-1}\mathbf{A} - \mathbf{B}(\mathbf{B}^\top\mathbf{B})^{-1}\mathbf{B}^\top\mathbf{Z}\mathbf{A}^\top(\mathbf{A}\mathbf{A}^\top)^{-1}\mathbf{A}.$$

1350 *Proof.* Suppose \mathbf{W} has a compact singular value decomposition, given by $\mathbf{W} = \mathbf{U}\Sigma\mathbf{V}^\top$, where
 1351 $\mathbf{U} \in \mathbb{R}^{m \times r}$, $\Sigma \in \mathbb{R}^{r \times r}$, $\mathbf{V} \in \mathbb{R}^{n \times r}$. Then the tangent space \mathbb{T}_W at \mathbf{W} is characterized as
 1352

$$1353 \quad \mathbb{T}_W = \{\mathbf{U}\mathbf{M}^\top + \mathbf{N}\mathbf{V}^\top, \text{ for } \mathbf{M} \in \mathbb{R}^{m \times r}, \mathbf{N} \in \mathbb{R}^{n \times r}\}.$$

1354 Therefore, the orthogonal projection of \mathbf{Z} onto \mathbb{T}_W is known to be (Wei et al., 2016)
 1355

$$1356 \quad \mathcal{P}_{\mathbb{T}_W}(\mathbf{Z}) = \mathbf{U}\mathbf{U}^\top \mathbf{Z} + \mathbf{Z}\mathbf{V}^\top \mathbf{V} - \mathbf{U}\mathbf{U}^\top \mathbf{Z}\mathbf{V}^\top \mathbf{V}. \quad (14)$$

1357 Since the columns of \mathbf{B} and \mathbf{U} span the same column space (i.e., the column space of \mathbf{W}), then there
 1358 exists an invertible matrix $\mathbf{S} \in \mathbb{R}^{r \times r}$ such that $\mathbf{B} = \mathbf{U}\mathbf{S}$ and $\mathbf{U} = \mathbf{B}\mathbf{S}^{-1}$. Using this relation, we
 1359 have
 1360

$$1361 \quad \mathbf{U}^\top \mathbf{U} = (\mathbf{B}\mathbf{S}^{-1})^\top \mathbf{B}\mathbf{S}^{-1} = \mathbf{S}^{-\top}(\mathbf{B}^\top \mathbf{B})\mathbf{S}^{-1}.$$

1362 Since $\mathbf{U}^\top \mathbf{U} = \mathbf{I}_r$, it follows that
 1363

$$1364 \quad \mathbf{S}^{-\top}(\mathbf{B}^\top \mathbf{B})\mathbf{S}^{-1} = \mathbf{I}_r \implies \mathbf{B}^\top \mathbf{B} = \mathbf{S}^\top \mathbf{S}.$$

1365 Using this, we compute $\mathbf{U}\mathbf{U}^\top$

$$1366 \quad \mathbf{U}\mathbf{U}^\top = \mathbf{B}\mathbf{S}^{-1}\mathbf{S}^{-\top}\mathbf{B} = \mathbf{B}(\mathbf{S}^\top \mathbf{S})^{-1}\mathbf{B}^\top = \mathbf{B}(\mathbf{B}^\top \mathbf{B})^{-1}\mathbf{B}^\top \quad (15)$$

1368 Similarly, since the rows of \mathbf{A} and the columns of \mathbf{V} span the same row space (i.e., the row space of
 1369 \mathbf{W}), there exists an invertible matrix $\mathbf{Q} \in \mathbb{R}^{r \times r}$ such that $\mathbf{A} = \mathbf{Q}\mathbf{V}^\top$ and $\mathbf{V}^\top = \mathbf{Q}^{-1}\mathbf{A}$. Further,
 1370 using $\mathbf{V}^\top \mathbf{V} = \mathbf{I}_r$, we obtain

$$1371 \quad \mathbf{V}^\top \mathbf{V} = \mathbf{Q}^{-1}(\mathbf{A}\mathbf{A}^\top)\mathbf{Q}^{-\top} = \mathbf{I}_r,$$

1373 hence $\mathbf{A}\mathbf{A}^\top = \mathbf{Q}\mathbf{Q}^\top$ and
 1374

$$1375 \quad \mathbf{V}\mathbf{V}^\top = \mathbf{A}^\top \mathbf{Q}^{-\top} \mathbf{Q}^{-1} \mathbf{A} = \mathbf{A}^\top (\mathbf{Q}\mathbf{Q}^\top)^{-1} \mathbf{A} = \mathbf{A}^\top (\mathbf{A}\mathbf{A}^\top)^{-1} \mathbf{A} \quad (16)$$

1376 Substituting (15) and (16) into (14) yields
 1377

$$1378 \quad \mathcal{P}_{\mathbb{T}_W}(\mathbf{Z}) = \mathbf{B}(\mathbf{B}^\top \mathbf{B})^{-1}\mathbf{B}^\top \mathbf{Z} + \mathbf{Z}\mathbf{A}^\top (\mathbf{A}\mathbf{A}^\top)^{-1} \mathbf{A} - \mathbf{B}(\mathbf{B}^\top \mathbf{B})^{-1}\mathbf{B}^\top \mathbf{Z}\mathbf{A}^\top (\mathbf{A}\mathbf{A}^\top)^{-1} \mathbf{A}.$$

1379 \square

1381 **Proposition D.3** (Orthogonal Projection onto the Tangent Space Under the Weighted Metric). *Let*
 1382 *$\mathbf{W} \in \mathcal{M}_r$ has a low-rank decomposition $\mathbf{W} = \mathbf{B}\mathbf{A}$, where $\mathbf{B} \in \mathbb{R}^{m \times r}$, $\mathbf{A} \in \mathbb{R}^{r \times n}$. Denote the*
 1383 *tangent space of the Riemannian manifold \mathcal{M}_r at the point \mathbf{W} as \mathbb{T}_W . The weighted metric is*
 1384 *defined as $\langle \mathbf{Y}, \mathbf{Z} \rangle_H = \langle \mathbf{L}^{\frac{1}{2}} \mathbf{Y} \mathbf{R}^{\frac{1}{2}}, \mathbf{Z} \rangle$ for any $\mathbf{Y}, \mathbf{Z} \in \mathbb{R}^{m \times n}$. Then, the orthogonal projection of*
 1385 *any matrix $\mathbf{Z} \in \mathbb{R}^{m \times n}$ onto \mathbb{T}_W under the weighed metric is given by*

$$1386 \quad \mathcal{P}_{\mathbb{T}_W}(\mathbf{Z}) = \mathbf{B}(\mathbf{B}^\top \mathbf{L}^{\frac{1}{2}} \mathbf{B})^{-1}\mathbf{B}^\top \mathbf{L}^{\frac{1}{2}} \mathbf{Z} + \mathbf{Z}\mathbf{R}^{\frac{1}{2}} \mathbf{A}^\top (\mathbf{A}\mathbf{R}^{\frac{1}{2}} \mathbf{A}^\top)^{-1} \mathbf{A}$$

$$1388 \quad - \mathbf{B}(\mathbf{B}^\top \mathbf{B})^{-1}\mathbf{B}^\top \mathbf{L}^{\frac{1}{2}} \mathbf{Z}\mathbf{R}^{\frac{1}{2}} \mathbf{A}^\top (\mathbf{A}\mathbf{A}^\top)^{-1} \mathbf{A}.$$

1390 *Proof.* This proof is inspired by (Bian et al., 2024). Here, we briefly provide a sketch of the proof.
 1391

1392 (i) *The new orthonormal basis under the weighted metric.* Let $\mathbf{W} = \mathbf{U}\Sigma\mathbf{V}^\top$ be a compact
 1393 SVD with $\mathbf{U} = [\mathbf{u}_1, \mathbf{u}_2, \dots, \mathbf{u}_r] \in \mathbb{R}^{m \times r}$, $\mathbf{V} = [\mathbf{v}_1, \mathbf{v}_2, \dots, \mathbf{v}_r] \in \mathbb{R}^{n \times r}$. Normalize the
 1394 singular vectors under the weighted vector
 1395

$$1396 \quad \langle \mathbf{x}, \mathbf{y} \rangle_{\mathbf{L}^{\frac{1}{2}}} = \langle \mathbf{L}^{\frac{1}{2}}\mathbf{x}, \mathbf{y} \rangle \text{ in } \mathbb{R}^m \quad \text{and} \quad \langle \mathbf{x}, \mathbf{y} \rangle_{\mathbf{R}^{\frac{1}{2}}} = \langle \mathbf{R}^{\frac{1}{2}}\mathbf{x}, \mathbf{y} \rangle \text{ in } \mathbb{R}^n$$

1397 to obtain
 1398

$$1399 \quad \widetilde{\mathbf{U}} = \mathbf{U}(\mathbf{U}^\top \mathbf{L}^{\frac{1}{2}} \mathbf{U})^{-\frac{1}{2}} := [\tilde{\mathbf{u}}_1, \tilde{\mathbf{u}}_2, \dots, \tilde{\mathbf{u}}_r] \in \mathbb{R}^{m \times r},$$

$$1400 \quad \widetilde{\mathbf{V}} = \mathbf{V}(\mathbf{V}^\top \mathbf{R}^{\frac{1}{2}} \mathbf{V})^{-\frac{1}{2}} := [\tilde{\mathbf{v}}_1, \tilde{\mathbf{v}}_2, \dots, \tilde{\mathbf{v}}_r] \in \mathbb{R}^{n \times r}.$$

1402 Next, we extend $\widetilde{\mathbf{U}}$ and $\widetilde{\mathbf{V}}$ to full orthonormal basis of $(\mathbb{R}^m, \langle \cdot, \cdot \rangle_{\mathbf{L}^{\frac{1}{2}}})$ and $(\mathbb{R}^n, \langle \cdot, \cdot \rangle_{\mathbf{R}^{\frac{1}{2}}})$ re-
 1403 spectively. Then, an orthonormal basis of \mathbb{T}_W with respect to $\langle \cdot, \cdot \rangle_{\mathbf{H}_t}$ is $\{\tilde{\mathbf{u}}_i \tilde{\mathbf{v}}_j^\top\}_{\min\{i,j\} \leq r}$.

1404 (ii) *Orthogonal projection represented by the new orthonormal basis.* Using the orthonormal
 1405 bases $\tilde{\mathbf{U}}$ and $\tilde{\mathbf{V}}$, the projection of \mathbf{Z} onto $\mathbb{T}_{\mathbf{W}}$ is expressed as:
 1406

$$\begin{aligned} 1407 \quad \tilde{\mathcal{P}}_{\mathbb{T}_{\mathbf{W}}}(\mathbf{Z}) &= \sum_{(i,j):\min\{i,j\} \leq r} \langle \mathbf{Z}, \tilde{\mathbf{u}}_i \tilde{\mathbf{v}}_j^\top \rangle_{\mathbf{H}_t} \cdot \tilde{\mathbf{u}}_i \tilde{\mathbf{v}}_j^\top = \sum_{(i,j):\min\{i,j\} \leq r} \langle \mathbf{L}^{\frac{1}{2}} \mathbf{Z} \mathbf{R}^{\frac{1}{2}}, \tilde{\mathbf{u}}_i \tilde{\mathbf{v}}_j^\top \rangle \cdot \tilde{\mathbf{u}}_i \tilde{\mathbf{v}}_j^\top \\ 1408 &= \sum_{(i,j):\min\{i,j\} \leq r} \tilde{\mathbf{u}}_i^\top \mathbf{L}^{\frac{1}{2}} \mathbf{Z} \mathbf{R}^{\frac{1}{2}} \tilde{\mathbf{v}}_j \cdot \tilde{\mathbf{u}}_i \tilde{\mathbf{v}}_j^\top \\ 1409 &= \tilde{\mathbf{U}} \tilde{\mathbf{U}}^\top \mathbf{L}^{\frac{1}{2}} \mathbf{Z} + \mathbf{Z} \mathbf{R}^{\frac{1}{2}} \tilde{\mathbf{V}} \tilde{\mathbf{V}}^\top - \tilde{\mathbf{U}} \tilde{\mathbf{U}}^\top \mathbf{L}^{\frac{1}{2}} \mathbf{Z} \mathbf{R}^{\frac{1}{2}} \tilde{\mathbf{V}} \tilde{\mathbf{V}}^\top. \\ 1410 \\ 1411 \\ 1412 \\ 1413 \end{aligned}$$

1414 (iii) *Express the basis projectors via factors \mathbf{B} and \mathbf{A} .* Since \mathbf{B} and \mathbf{A} span the same spaces as
 1415 \mathbf{U} and \mathbf{V} , we derive

$$1416 \quad \tilde{\mathbf{U}} \tilde{\mathbf{U}}^\top = \mathbf{B} \left(\mathbf{B}^\top \mathbf{L}^{\frac{1}{2}} \mathbf{B} \right)^{-1} \mathbf{B}^\top, \quad \tilde{\mathbf{V}} \tilde{\mathbf{V}}^\top = \mathbf{A}^\top \left(\mathbf{A} \mathbf{R}^{\frac{1}{2}} \mathbf{A}^\top \right)^{-1} \mathbf{A}. \\ 1417 \\ 1418$$

1419 Substituting these expressions into the formula for $\tilde{\mathcal{P}}_{\mathbb{T}_{\mathbf{W}}}$, we obtain

$$\begin{aligned} 1420 \quad \tilde{\mathcal{P}}_{\mathbb{T}_{\mathbf{W}}}(\mathbf{Z}) &= \mathbf{B} \left(\mathbf{B}^\top \mathbf{L}^{\frac{1}{2}} \mathbf{B} \right)^{-1} \mathbf{B}^\top \mathbf{L}^{\frac{1}{2}} \mathbf{Z} + \mathbf{Z} \mathbf{R}^{\frac{1}{2}} \mathbf{A}^\top \left(\mathbf{A} \mathbf{R}^{\frac{1}{2}} \mathbf{A}^\top \right)^{-1} \mathbf{A} \\ 1421 &\quad - \mathbf{B} \left(\mathbf{B}^\top \mathbf{L}^{\frac{1}{2}} \mathbf{B} \right)^{-1} \mathbf{B}^\top \mathbf{L}^{\frac{1}{2}} \mathbf{Z} \mathbf{R}^{\frac{1}{2}} \mathbf{A}^\top \left(\mathbf{A} \mathbf{R}^{\frac{1}{2}} \mathbf{A}^\top \right)^{-1} \mathbf{A}. \\ 1422 \\ 1423 \\ 1424 \end{aligned} \quad \square$$

1425 **Proposition D.4.** Suppose $\mathbf{W} \in \mathcal{M}_r$ has a low-rank decomposition $\mathbf{W} = \mathbf{B}\mathbf{A}$, where $\mathbf{B} \in \mathbb{R}^{m \times r}$
 1426 and $\mathbf{A} \in \mathbb{R}^{r \times n}$. For any matrix $\mathbf{M} \in \mathbb{R}^{m \times r}$, $\mathbf{N} \in \mathbb{R}^{r \times n}$, the matrix $\mathbf{M}\mathbf{A} + \mathbf{B}\mathbf{N}$ lies in the tangent
 1427 space $\mathbb{T}_{\mathbf{W}}$ at \mathbf{W} of \mathcal{M}_r at the point \mathbf{W} .

1429 *Proof.* Let $\mathbf{W} \in \mathcal{M}_r$ has a compact singular value decomposition $\mathbf{W} = \mathbf{U}\Sigma\mathbf{V}^\top$, where $\mathbf{U} \in \mathbb{R}^{m \times r}$,
 1430 $\Sigma \in \mathbb{R}^{r \times r}$, and $\mathbf{V} \in \mathbb{R}^{n \times r}$. By definition, the tangent space $\mathbb{T}_{\mathbf{W}}$ at \mathbf{W} is given by

$$1432 \quad \mathbb{T}_{\mathbf{W}} = \{ \mathbf{U}\mathbf{K}_1^\top + \mathbf{K}_2\mathbf{V}^\top \mid \mathbf{K}_1 \in \mathbb{R}^{n \times r}, \mathbf{K}_2 \in \mathbb{R}^{m \times r} \}.$$

1433 Since \mathbf{B} and \mathbf{A} are low-rank factors of \mathbf{W} , there exist invertible matrices $\mathbf{S} \in \mathbb{R}^{r \times r}$ and $\mathbf{Q} \in \mathbb{R}^{r \times r}$
 1434 such that

$$1435 \quad \mathbf{B} = \mathbf{U}\mathbf{S}, \quad \mathbf{A} = \mathbf{Q}\mathbf{V}^\top.$$

1436 Substituting these expressions, the matrix $\mathbf{M}\mathbf{A} + \mathbf{B}\mathbf{N}$ can be rewritten as

$$1438 \quad \mathbf{M}\mathbf{A} + \mathbf{B}\mathbf{N} = \mathbf{M}\mathbf{Q}\mathbf{V}^\top + \mathbf{U}\mathbf{S}\mathbf{N}.$$

1439 The first term, $\mathbf{M}\mathbf{Q}\mathbf{V}^\top$, lies in $\text{span}(\mathbf{V}^\top)$, and the second term, $\mathbf{U}\mathbf{S}\mathbf{N}$, lies in $\text{span}(\mathbf{U})$. Thus, the
 1440 sum $\mathbf{M}\mathbf{Q}\mathbf{V}^\top + \mathbf{U}\mathbf{S}\mathbf{N}$ lies in the tangent space $\mathbb{T}_{\mathbf{W}}$ by the definition of the tangent space. Then, it
 1441 follows that $\mathbf{M}\mathbf{A} + \mathbf{B}\mathbf{N}$ is on the tangent space $\mathbb{T}_{\mathbf{W}}$. This completes the proof. \square

1443 D.3 PROOFS OF THEOREM 3.1 AND THEOREM 3.2

1445 **Proof of Theorem 3.1.** Define

$$1446 \quad \Gamma(\Delta_{\mathbf{B}_t}, \Delta_{\mathbf{A}_t}) := \frac{1}{2} \|\Delta_{\mathbf{B}_t} \mathbf{A}_t + \mathbf{B}_t \Delta_{\mathbf{A}_t} - \tilde{\mathcal{P}}_{\mathbb{T}_t}(\mathbf{L}_t^{-\frac{1}{2}} \mathbf{G}_t \mathbf{R}_t^{-\frac{1}{2}})\|_{\mathbf{H}_t}^2.$$

1449 Differentiating $\Gamma(\Delta_{\mathbf{B}_t}, \Delta_{\mathbf{A}_t})$ with respect to $\Delta_{\mathbf{B}_t}$ and $\Delta_{\mathbf{A}_t}$ yields

$$1450 \quad \nabla_{\Delta_{\mathbf{B}_t}} \Gamma(\Delta_{\mathbf{B}_t}, \Delta_{\mathbf{A}_t}) = \mathbf{L}_t^{\frac{1}{2}} \Delta_{\mathbf{B}_t} (\mathbf{A}_t \mathbf{R}_t^{\frac{1}{2}} \mathbf{A}_t^\top) + \mathbf{L}_t^{\frac{1}{2}} \mathbf{B}_t \Delta_{\mathbf{A}_t} \mathbf{R}_t^{\frac{1}{2}} \mathbf{A}_t^\top - \mathbf{G}_t \mathbf{A}_t^\top, \quad (17)$$

1452 and

$$1454 \quad \nabla_{\Delta_{\mathbf{A}_t}} \Gamma(\Delta_{\mathbf{B}_t}, \Delta_{\mathbf{A}_t}) = \mathbf{B}_t^\top \mathbf{L}_t^{\frac{1}{2}} \Delta_{\mathbf{B}_t} \mathbf{A}_t \mathbf{R}_t^{\frac{1}{2}} + \mathbf{B}_t^\top \mathbf{L}_t^{\frac{1}{2}} \mathbf{B}_t \Delta_{\mathbf{A}_t} \mathbf{R}_t^{\frac{1}{2}} - \mathbf{B}_t^\top \mathbf{G}_t. \quad (18)$$

1455 Setting $\nabla_{\Delta_{\mathbf{B}_t}} \Gamma(\Delta_{\mathbf{B}_t}, \Delta_{\mathbf{A}_t}) = \mathbf{0}$ and using the invertibility of $(\mathbf{A}_t \mathbf{R}_t^{\frac{1}{2}} \mathbf{A}_t^\top)$ and $\mathbf{L}_t^{\frac{1}{2}}$ gives

$$1457 \quad \Delta_{\mathbf{B}_t} = \mathbf{L}_t^{-\frac{1}{2}} \mathbf{G}_t \mathbf{A}_t^\top (\mathbf{A}_t \mathbf{R}_t^{\frac{1}{2}} \mathbf{A}_t^\top)^{-1} - \mathbf{B}_t \Delta_{\mathbf{A}_t} \mathbf{R}_t^{\frac{1}{2}} \mathbf{A}_t^\top (\mathbf{A}_t \mathbf{R}_t^{\frac{1}{2}} \mathbf{A}_t^\top)^{-1}. \quad (19)$$

1458 Substituting (18) into $\nabla_{\Delta_{A_t}} \Gamma(\Delta_{B_t}, \Delta_{A_t}) = \mathbf{0}$ and using the invertibility of $B_t^\top L_t^{\frac{1}{2}} B_t$ and $R_t^{\frac{1}{2}}$
 1459 yields
 1460

$$\Delta_{A_t} [\mathbf{I} - \tilde{Q}_{A_t}] = (B_t^\top L_t^{\frac{1}{2}} B_t)^{-1} B_t^\top G_t R_t^{-\frac{1}{2}} [\mathbf{I} - \tilde{Q}_{A_t}],$$

1462 where $\tilde{Q}_{A_t} = R_t^{\frac{1}{2}} A_t^\top (A_t R_t^{\frac{1}{2}} A_t^\top)^{-1} A_t$, which is the projection matrix onto the row space of A_t .
 1463 Since $\mathbf{I} - \tilde{Q}_{A_t}$ is the residual maker matrix, then a general solution is
 1464

$$\Delta_{A_t}^{\text{opt}} = (B_t^\top L_t^{\frac{1}{2}} B_t)^{-1} B_t^\top G_t R_t^{-\frac{1}{2}} + X_t A_t,$$

1465 with arbitrary matrix $X_t \in \mathbb{R}^{r \times r}$. Plugging this Δ_{A_t} back into (19) gives
 1466

$$\Delta_{B_t}^{\text{opt}} = [\mathbf{I} - \tilde{P}_{B_t}] L_t^{-\frac{1}{2}} G_t A_t^\top (A_t R_t^{\frac{1}{2}} A_t^\top)^{-1} - B_t X_t,$$

1467 where $\tilde{P}_{B_t} = B_t (B_t^\top L_t^{\frac{1}{2}} B_t)^{-1} B_t^\top L_t^{\frac{1}{2}}$, which is the projection matrix onto the column space of B_t .
 1468 \square
 1469

1470 **Proof of Theorem 3.2.** Let the objective function be $\Psi(X_t) = \frac{1}{2} \|\Delta_{B_t} A_t - B_t \Delta_{A_t}\|_{H_t}^2$. To
 1471 minimize $\Psi(X_t)$, we compute its gradient with respect to X_t ,
 1472

$$\nabla_{X_t} \Psi(X_t) = B_t^\top L_t^{\frac{1}{2}} (\Delta_{B_t} A_t - B_t \Delta_{A_t}) R_t^{\frac{1}{2}} A^\top.$$

1473 Substituting the expressions for A_t and B_t from Theorem 3.1, we have
 1474

$$\begin{aligned} \nabla_{X_t} \Psi(X_t) &= B_t^\top L_t^{\frac{1}{2}} \left([\mathbf{I} - B_t (B_t^\top L_t^{\frac{1}{2}} B_t)^{-1} B_t^\top L_t^{\frac{1}{2}}] L_t^{-\frac{1}{2}} G_t A_t^\top (A_t R_t^{\frac{1}{2}} A_t^\top)^{-1} A_t \right. \\ &\quad \left. - B_t (B_t^\top L_t^{\frac{1}{2}} B_t)^{-1} B_t^\top G_t R_t^{-\frac{1}{2}} - 2 B_t X_t A_t \right) R_t^{\frac{1}{2}} A^\top \\ &= -B_t^\top G_t A_t - 2(B_t^\top L_t^{\frac{1}{2}} B_t) X_t (A_t R_t^{\frac{1}{2}} A_t^\top). \end{aligned}$$

1475 Setting $\nabla_{X_t} \Psi(X_t) = \mathbf{0}$, we obtain
 1476

$$-B_t^\top G_t A_t = 2(B_t^\top L_t^{\frac{1}{2}} B_t) X_t (A_t R_t^{\frac{1}{2}} A_t^\top).$$

1477 Since $B_t^\top L_t^{\frac{1}{2}} B_t$ and $A_t R_t^{\frac{1}{2}} A_t^\top$ are invertible, we solve for X_t as
 1478

$$X_t^{\text{opt}} = -\frac{1}{2} (B_t^\top L_t^{\frac{1}{2}} B_t)^{-1} B_t^\top G_t A_t^\top (A_t R_t^{\frac{1}{2}} A_t^\top)^{-1}.$$

1479 Thus, the optimal solution for X_t is derived. \square
 1480

1481 D.4 PROOF OF THE LOSS FUNCTION EXHIBITS A DECREASING TREND

1482 Under the framework of LoRA, the infinitesimal change in loss is
 1483

$$\begin{aligned} d\mathcal{L} &= \langle G_B, dB \rangle_H + \langle G_A, dA \rangle_H \\ &= -\eta (\langle G_B, \Delta_B \rangle_H + \langle G_A, \Delta_A \rangle_H) \\ &= -\eta \left(\langle G_B, [\mathbf{I} - B(B^\top L^{\frac{1}{2}} B)^{-1} B^\top L^{\frac{1}{2}}] L^{-\frac{1}{2}} G_B (A R^{\frac{1}{2}} A^\top)^{-1} - B X \rangle_H \right. \\ &\quad \left. + \langle G_A, (B^\top L^{\frac{1}{2}} B)^{-1} G_A R^{-\frac{1}{2}} + X A \rangle_H \right) \\ &= -\eta \left(\langle G_B, [\mathbf{I} - B(B^\top L^{\frac{1}{2}} B)^{-1} B^\top L^{\frac{1}{2}}] L^{-\frac{1}{2}} G_B (A R^{\frac{1}{2}} A^\top)^{-1} \rangle_H + \langle G_A, (B^\top L^{\frac{1}{2}} B)^{-1} G_A R^{-\frac{1}{2}} \rangle_H \right. \\ &\quad \left. + \langle G_B, -B X \rangle_H + \langle G_A, X A \rangle_H \right) \\ &= -\eta \left(\langle G_B, [\mathbf{I} - B(B^\top L^{\frac{1}{2}} B)^{-1} B^\top L^{\frac{1}{2}}] L^{-\frac{1}{2}} G_B (A R^{\frac{1}{2}} A^\top)^{-1} \rangle_H + \langle G_A, (B^\top L^{\frac{1}{2}} B)^{-1} G_A R^{-\frac{1}{2}} \rangle_H \right), \end{aligned} \quad (20)$$

1512 Where the third line is derived from Theorem 3.1, the forth line is because of the additivity of the
 1513 inner product, and the last line is because
 1514

$$\begin{aligned}
 1515 \langle \mathbf{G}_B, -\mathbf{B}\mathbf{X} \rangle_H + \langle \mathbf{G}_A, \mathbf{X}\mathbf{A} \rangle_H &= \langle -\mathbf{B}^\top \mathbf{G}_B + \mathbf{G}_A \mathbf{A}^\top, \mathbf{X} \rangle_H \\
 1516 &= \langle -\mathbf{B}^\top \mathbf{G}\mathbf{A}^\top + \mathbf{B}^\top \mathbf{G}\mathbf{A}^\top, \mathbf{X} \rangle_H \\
 1517 &= 0.
 \end{aligned}$$

1518 Therefore, to prove $d\mathcal{L} \leq 0$, it suffices to prove that
 1519

$$\begin{aligned}
 1520 \langle \mathbf{G}_B, [\mathbf{I} - \mathbf{B}(\mathbf{B}^\top \mathbf{L}^{\frac{1}{2}} \mathbf{B})^{-1} \mathbf{B}^\top \mathbf{L}^{\frac{1}{2}} \mathbf{L}^{-\frac{1}{2}} \mathbf{G}_B (\mathbf{A}\mathbf{R}^{\frac{1}{2}} \mathbf{A}^\top)^{-1}] \rangle_H &\geq 0, \\
 1521 \langle \mathbf{G}_A, (\mathbf{B}^\top \mathbf{L}^{\frac{1}{2}} \mathbf{B})^{-1} \mathbf{G}_A \mathbf{R}^{-\frac{1}{2}} \rangle_H &\geq 0.
 \end{aligned}$$

1524 1. First to prove $\langle \mathbf{G}_B, [\mathbf{I} - \mathbf{B}(\mathbf{B}^\top \mathbf{L}^{\frac{1}{2}} \mathbf{B})^{-1} \mathbf{B}^\top \mathbf{L}^{\frac{1}{2}}] \mathbf{L}^{-\frac{1}{2}} \mathbf{G}_B (\mathbf{A}\mathbf{R}^{\frac{1}{2}} \mathbf{A}^\top)^{-1} \rangle_H \geq 0$.
 1525

- 1526 • Prove $[\mathbf{I} - \mathbf{B}(\mathbf{B}^\top \mathbf{L}^{\frac{1}{2}} \mathbf{B})^{-1} \mathbf{B}^\top \mathbf{L}^{\frac{1}{2}}]$ is symmetric and positive semi-definite.
 1527 From Equation (10), we have $\tilde{\mathbf{P}}_B = \mathbf{B}(\mathbf{B}^\top \mathbf{L}^{\frac{1}{2}} \mathbf{B})^{-1} \mathbf{B}^\top \mathbf{L}^{\frac{1}{2}}$. $\tilde{\mathbf{P}}_B$ is symmetric in the
 1528 weighted space if it is self-adjoint with respect to the weighted inner product. That
 1529 means we need to prove for all vectors $\mathbf{x}, \mathbf{y} \in \mathbb{R}^m$

$$\langle \tilde{\mathbf{P}}_B \mathbf{x}, \mathbf{y} \rangle_H = \langle \mathbf{x}, \tilde{\mathbf{P}}_B \mathbf{y} \rangle_H$$

1532 For the left-hand side,

$$\langle \tilde{\mathbf{P}}_B \mathbf{x}, \mathbf{y} \rangle_H = \langle \mathbf{L}^{\frac{1}{2}} \tilde{\mathbf{P}}_B \mathbf{x}, \mathbf{y} \rangle = \langle \mathbf{L}^{\frac{1}{2}} \mathbf{B}(\mathbf{B}^\top \mathbf{L}^{\frac{1}{2}} \mathbf{B})^{-1} \mathbf{B}^\top \mathbf{L}^{\frac{1}{2}} \mathbf{x}, \mathbf{y} \rangle.$$

1536 For the right-hand side,

$$\langle \mathbf{x}, \tilde{\mathbf{P}}_B \mathbf{y} \rangle_H = \langle \mathbf{L}^{\frac{1}{2}} \mathbf{x}, \tilde{\mathbf{P}}_B \mathbf{y} \rangle = \langle \tilde{\mathbf{P}}_B^\top \mathbf{L}^{\frac{1}{2}} \mathbf{x}, \mathbf{y} \rangle = \langle \mathbf{L}^{\frac{1}{2}} \mathbf{B}(\mathbf{B}^\top \mathbf{L}^{\frac{1}{2}} \mathbf{B})^{-1} \mathbf{B}^\top \mathbf{L}^{\frac{1}{2}} \mathbf{x}, \mathbf{y} \rangle.$$

1539 Thus, the left-hand side equals to the right-hand side, $\tilde{\mathbf{P}}_B$ is symmetric.
 1540 By Proposition D.3, $\tilde{\mathbf{P}}_B$ is the orthogonal projection under the inner product $\langle \cdot, \cdot \rangle_H$.
 1541 As a projection matrix, the eigenvalues of $\tilde{\mathbf{P}}_B$ are zeros and ones. Thus, $\tilde{\mathbf{P}}_B^\top$ and
 1542 $\mathbf{I} - \tilde{\mathbf{P}}_B^\top$ are both positive semi-definite matrices.
 1543

1544 There exists a Cholesky decomposition of $\mathbf{I} - \tilde{\mathbf{P}}_B^\top$, denote as $\mathbf{I} - \tilde{\mathbf{P}}_B^\top = \mathbf{K}\mathbf{K}^\top$,
 1545 where $\mathbf{K} \in \mathbb{R}^{m \times m}$ is a lower triangular matrix.

- 1546 • Prove $(\mathbf{A}\mathbf{R}^{\frac{1}{2}} \mathbf{A}^\top)^{-1}$ is symmetric and positive definite.
 1547 Since \mathbf{R} is a diagonal matrix, then symmetric, and therefore $\mathbf{A}\mathbf{R}^{\frac{1}{2}} \mathbf{A}^\top$ is also symmetric.
 1548

1549 For any non-zero vector $\mathbf{x} \in \mathbb{R}^r$, $\mathbf{x}^\top \mathbf{A}\mathbf{R}^{\frac{1}{2}} \mathbf{A}^\top \mathbf{x} = \langle \mathbf{A}^\top \mathbf{x}, \mathbf{A}^\top \mathbf{x} \rangle_H = \|\mathbf{A}^\top \mathbf{x}\|_H^2 > 0$.
 1550

1551 Thus, $\mathbf{A}\mathbf{R}^{\frac{1}{2}} \mathbf{A}^\top$ is a positive definite matrix.
 1552

1553 Therefore, $\mathbf{A}\mathbf{R}^{\frac{1}{2}} \mathbf{A}^\top$ is invertible and $(\mathbf{A}\mathbf{R}^{\frac{1}{2}} \mathbf{A}^\top)^{-1}$ is symmetric and positive definite.
 1554

1555 There exists a Cholesky decomposition of $(\mathbf{A}\mathbf{R}^{\frac{1}{2}} \mathbf{A}^\top)^{-1}$, denote as $(\mathbf{A}\mathbf{R}^{\frac{1}{2}} \mathbf{A}^\top)^{-1} = \mathbf{C}\mathbf{C}^\top$, where $\mathbf{C} \in \mathbb{R}^{r \times r}$ is a lower triangular matrix.
 1556

1557 Since $[\mathbf{I} - \mathbf{B}(\mathbf{B}^\top \mathbf{L}^{\frac{1}{2}} \mathbf{B})^{-1} \mathbf{B}^\top \mathbf{L}^{\frac{1}{2}}]$ and $(\mathbf{A}\mathbf{R}^{\frac{1}{2}} \mathbf{A}^\top)^{-1}$ both have a Cholesky decomposition.
 1558 The inner product can be rewritten as

$$\begin{aligned}
 1559 \langle \mathbf{G}_B, [\mathbf{I} - \mathbf{B}(\mathbf{B}^\top \mathbf{L}^{\frac{1}{2}} \mathbf{B})^{-1} \mathbf{B}^\top \mathbf{L}^{\frac{1}{2}}] \mathbf{L}^{-\frac{1}{2}} \mathbf{G}_B (\mathbf{A}\mathbf{R}^{\frac{1}{2}} \mathbf{A}^\top)^{-1} \rangle_H \\
 1560 &= \langle \mathbf{G}_B, \mathbf{K}\mathbf{K}^\top \mathbf{L}^{-\frac{1}{2}} \mathbf{G}_B \mathbf{C}\mathbf{C}^\top \rangle_H \\
 1561 &= \langle \mathbf{L}^{-\frac{1}{2}} \mathbf{K}\mathbf{K}^\top \mathbf{G}_B, \mathbf{G}_B \mathbf{C}\mathbf{C}^\top \rangle_H \\
 1562 &= \langle \mathbf{K}\mathbf{K}^\top \mathbf{G}_B, \mathbf{G}_B \mathbf{C}\mathbf{C}^\top \rangle \\
 1563 &= \langle \mathbf{K}^\top \mathbf{G}_B \mathbf{C}, \mathbf{K}^\top \mathbf{G}_B \mathbf{C} \rangle \\
 1564 &= \|\mathbf{K}^\top \mathbf{G}_B \mathbf{C}\|_F^2 \\
 1565 &\geq 0
 \end{aligned}$$

1566 2. Then prove $\langle \mathbf{G}_A, (\mathbf{B}^\top \mathbf{L}^{\frac{1}{2}} \mathbf{B})^{-1} \mathbf{G}_A \mathbf{R}^{-\frac{1}{2}} \rangle_H \geq 0$.

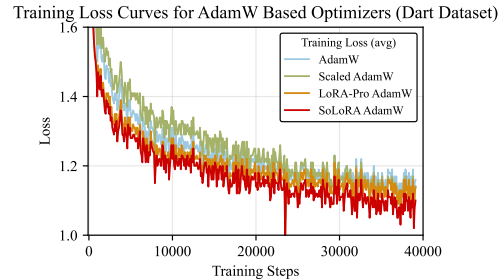
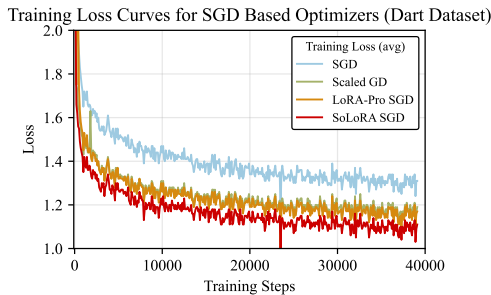
1567 Similar to $(\mathbf{A} \mathbf{R}^{\frac{1}{2}} \mathbf{A}^\top)^{-1}$ is symmetric and positive definite, $(\mathbf{B}^\top \mathbf{L}^{\frac{1}{2}} \mathbf{B})^{-1}$ is symmetric
 1568 positive definite, and there exists a Cholesky decomposition of $(\mathbf{B}^\top \mathbf{L}^{\frac{1}{2}} \mathbf{B})^{-1}$, denote as
 1569 $(\mathbf{B}^\top \mathbf{L}^{\frac{1}{2}} \mathbf{B})^{-1} = \mathbf{D} \mathbf{D}^\top$, where $\mathbf{D} \in \mathbb{R}^{r \times r}$ is a lower triangular matrix.

1570 Thus, the inner product can be rewritten as

$$\begin{aligned}
 & \langle \mathbf{G}_A, (\mathbf{B}^\top \mathbf{L}^{\frac{1}{2}} \mathbf{B})^{-1} \mathbf{G}_A \mathbf{R}^{-\frac{1}{2}} \rangle_H \\
 &= \langle \mathbf{G}_A, \mathbf{D} \mathbf{D}^\top \mathbf{G}_A \mathbf{R}^{-\frac{1}{2}} \rangle_H \\
 &= \langle \mathbf{G}_A \mathbf{R}^{\frac{1}{2}}, \mathbf{D} \mathbf{D}^\top \mathbf{G}_A \mathbf{R}^{-\frac{1}{2}} \rangle \\
 &= \langle \mathbf{G}_A, \mathbf{D} \mathbf{D}^\top \mathbf{G}_A \rangle \\
 &= \langle \mathbf{D}^\top \mathbf{G}_A, \mathbf{D}^\top \mathbf{G}_A \rangle \\
 &= \|\mathbf{D}^\top \mathbf{G}_A\|_F^2 \\
 &\geq 0
 \end{aligned}$$

1582 In the conclusion, we have completed the proof of $d\mathcal{L} \leq 0$. This ensures that the SoLoRA model
 1583 maintains a decreasing trend in the loss.

E ADDITIONAL EXPERIMENTS



(a) Training loss curve over training steps when fine-tuning using SGD-based method.

(b) Training loss curve over training time when fine-tuning using AdamW-based method.

1602 Figure 13: Training loss of GPT-2 small model ($r = 4$) fine-tuned using different optimizers.
 1603 Evaluation is conducted on the DART Dataset.

F THE USE OF LARGE LANGUAGE MODELS (LLMs)

1608 We use LLMs to polish writing.

1609
 1610
 1611
 1612
 1613
 1614
 1615
 1616
 1617
 1618
 1619